Cell Reports

Article

Reciprocal regulation of phosphatidylcholine synthesis and H3K36 methylation programs metabolic adaptation

Graphical abstract

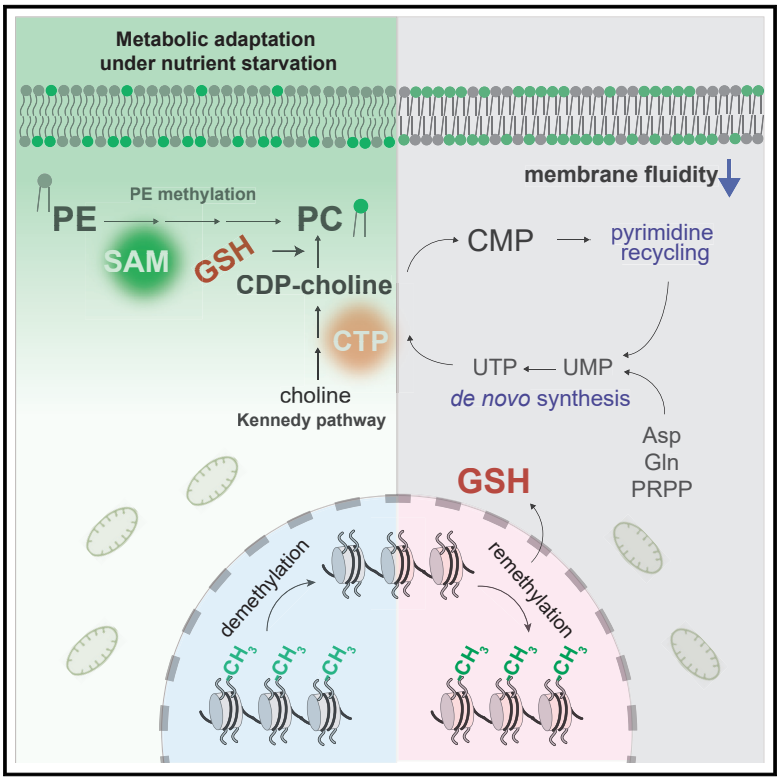

Highlights

- H3K36me deficiency sensitizes respiring cells to loss of viability under starvation
- Loss of H3K36me leads to membrane defects with aberrant phospholipid compositions
- The methyl sink function for H3K36 affects phospholipid and pyrimidine metabolism
- Rewiring phosphatidylcholine synthesis necessitates metabolic coordination

Authors

Wen Fang, Yibing Zhu, Sen Yang, Xiaomeng Tong, Cunqi Ye

Correspondence

yecunqi@zju.edu.cn

In brief

Fang et al. show an adaptive mechanism by which the nutrient-sensitive methylation of H3K36 plays a role in the metabolic balance of phospholipid synthesis and nucleotide metabolism in the redox environment.

Fang et al., 2022, Cell Reports *39*, 110672
April 12, 2022
https://doi.org/10.1016/j.celrep.2022.110672

CellPress

Cell Reports

CellPress
OPEN ACCESS

Article

Reciprocal regulation of phosphatidylcholine synthesis and H3K36 methylation programs metabolic adaptation

Wen Fang,[1,3] Yibing Zhu,[1,3] Sen Yang,[1] Xiaomeng Tong,[1] and Cunqi Ye[1,2,4,*]
[1]Zhejiang Provincial Key Laboratory for Cancer Molecular Cell Biology, Life Sciences Institute, Zhejiang University, Hangzhou, China
[2]Kidney Disease Center, The First Affiliated Hospital, Zhejiang University School of Medicine, Hangzhou, China
[3]These authors contributed equally
[4]Lead contact
*Correspondence: yecunqi@zju.edu.cn
https://doi.org/10.1016/j.celrep.2022.110672

SUMMARY

Phospholipid biosynthesis plays a role in mediating membrane-to-histone communication that influences metabolic decisions. Upon nutrient deprivation, phospholipid methylation generates a starvation signal in the form of *S*-adenosylmethionine (SAM) depletion, leading to dynamic changes in histone methylation. Here we show that the SAM-responsive methylation of H3K36 is critical for metabolic adaptation to nutrient starvation in the budding yeast *Saccharomyces cerevisiae*. We find that mutants deficient in H3K36 methylation exhibit defects in membrane integrity and pyrimidine metabolism and lose viability quickly under starvation. Adjusting the synthesis of phospholipids potently rewires metabolic pathways for nucleotide synthesis and boosts the production of antioxidants, ameliorating the defects resulting from the loss of H3K36 methylation. We further demonstrate that H3K36 methylation reciprocally regulates phospholipid synthesis by influencing redox balance. Our study illustrates an adaptive mechanism whereby phospholipid synthesis entails a histone modification to reprogram metabolism for adaptation in a eukaryotic model organism.

INTRODUCTION

The ability of cells to reprogram cellular metabolism is essential for their growth and survival in different environments. How lipid repertoire contributes to metabolic adaptation remains an open question. Cells invest substantial resources to build cellular membranes that consist primarily of proteins and lipids. The protein-containing lipid matrix approximates a phospholipid bilayer in which alterations in phospholipid composition can influence many membrane-associated functions, such as membrane fluidity, permeability, active solute transport, and membrane-protein interactions (van Meer et al., 2008; Zhang and Rock, 2008). Modifying phospholipid composition can serve as an adaptive mechanism by which membrane functions are adjusted to match environmental requirements. Under high temperatures, for example, bacterial cells make a large proportion of phospholipids containing saturated and long-chain fatty acids to maintain the fluidity of cellular membranes (Sinensky, 1974). This homeoviscous adaptation mechanism modulates the electron transport chain function and minimizes energy expenditure, leading to optimized cell growth (Budin et al., 2018).

The synthesis of phospholipids, including aliphatic chains, polar head groups, and the glycerol backbone, intertwines with various metabolic pathways to supply intermediary metabolites, many of which can perform regulatory functions. Therefore, producing phospholipid biomass may drive the metabolic transformation to enable an adaptive mechanism. For example, the glycerol-3-phosphate shuttle that provides glycerol backbones for phospholipids and the synthesis of highly unsaturated fatty acids both can modulate redox homeostasis by regenerating nicotinamide adenosine dinucleotide (NAD+) (Kim et al., 2019; Liu et al., 2021). Also, *de novo* lipogenesis uses while fatty acid oxidation produces acetyl-coenzyme A (CoA), a central metabolite whose abundance dictates histone acetylation for gene regulation (Cai et al., 2011; Comerford et al., 2014; Hsieh et al., 2022; Koundouros and Poulogiannis, 2020; Sivanand et al., 2018).

Our previous studies demonstrated SAM-assisted crosstalk between membrane phospholipids and the epigenome (Ye et al., 2017, 2019). However, what necessitates the coordination between phospholipid and histone methylation remains elusive. Using the budding yeast as a model organism, we show an adaptive mechanism relying on this crosstalk. We find that H3K36 methylation deficiency sensitizes respiring cells to losing viability under nutrient starvation. The mutants deficient in H3K36 methylation exhibit membrane defects with aberrant phospholipid compositions, revealing an unprecedented role of H3K36 methylation in maintaining membrane integrity. We show that loss of H3K36 methylation leads to an oxidation-responsive inhibition of the CTP-requiring Kennedy pathway for phosphatidylcholine (PC) synthesis, resounding with the methyl group sink role of the histone H3K36 in the nucleus. Such inhibition results in an intermediary metabolite CDP-choline accumulation,

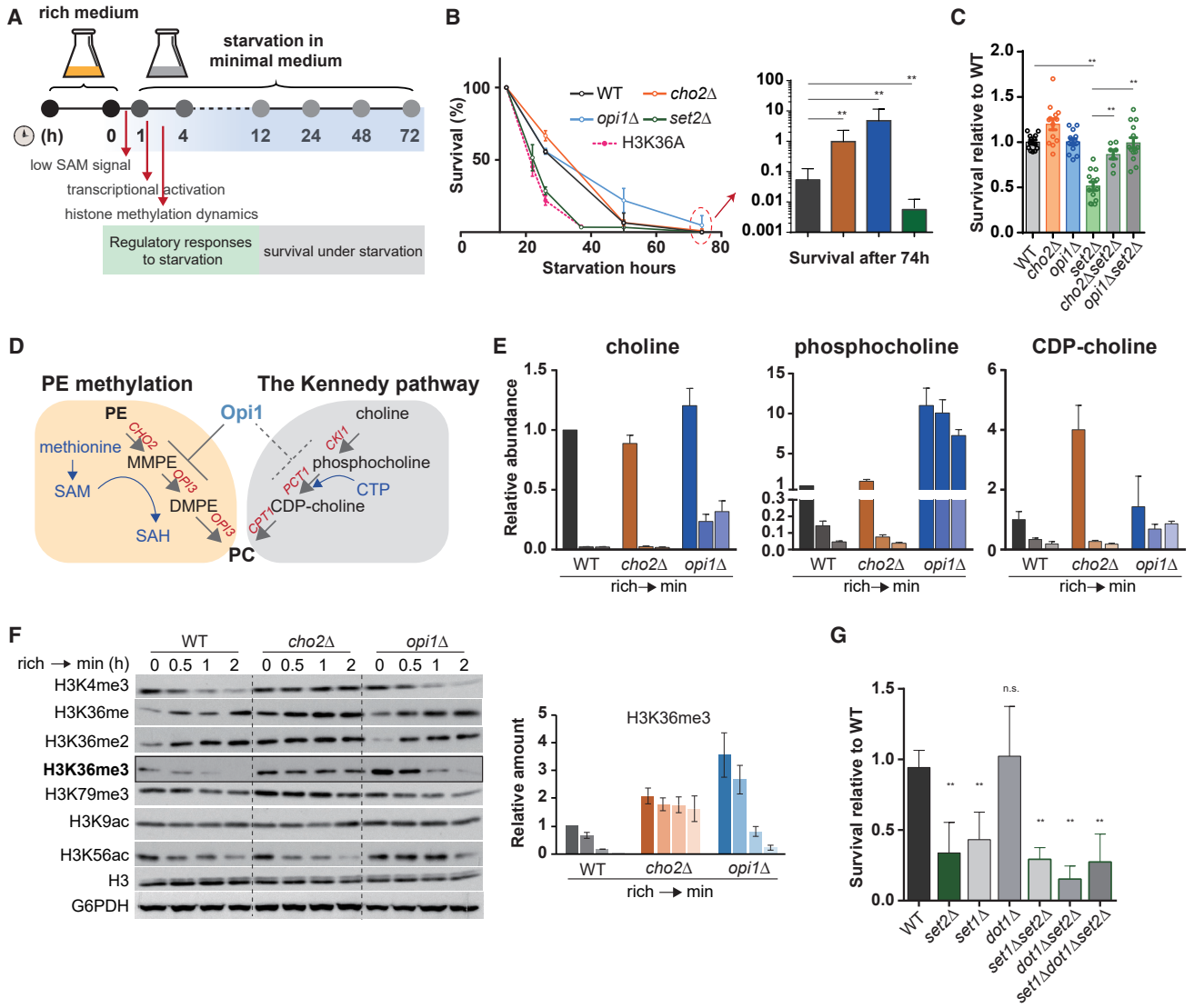

Figure 1. Loss of H3K36 methylation decreased survival rates under starvation, which was ameliorated by the mutants adjusting phospholipid synthesis

(A) Schematic of the experimental design.

(B and C) Survival rates of indicated mutants under starvation. Data are presented as mean ± SD ($n \geq 3$). **$p < 0.01$.

(D) PC synthesis pathways.

(E) Choline, phosphocholine, and CDP-choline abundances. Data are represented as mean ± SD ($n = 3$).

(F) Left: western blot assaying histone modifications in WT and mutant cells before and after the switch. Right: quantitative analysis of H3K36me3 amounts.

(G) Relative survival rates of a single or combinatorial deletion of histone methyltransferases. Data are presented as mean ± SD ($n \geq 3$). **$p < 0.01$.

forming a pyrimidine cache that diminishes pyrimidine recycling. H3K36 methylation deficiency leads to an imbalance in purine and pyrimidine metabolism along with the SAM turnover defect. This maladaptation to starvation can be alleviated by genetically reprogramming PC biosynthesis pathways. This is because rewiring phospholipid metabolism under starvation adjusts membrane phospholipid compositions, drives a metabolic flow for nucleotide biosynthesis, and enhances the production of antioxidant metabolites, such as GSH. Such survival advantages fortify cellular capacity to defend adaptive stress.

RESULTS

Loss of H3K36 methylation exhibited survival deficiency under starvation, which was suppressed by the mutants rewiring phospholipid synthesis

We previously established a starvation regimen by switching respiring yeast cells growing in lactate-based rich medium (rich) to lactate-based minimal medium (min) (Figure 1A). We found that cellular methionine and SAM serve as metabolic signals of nutrient sufficiency that regulate autophagy (Sutter

CellPress
OPEN ACCESS

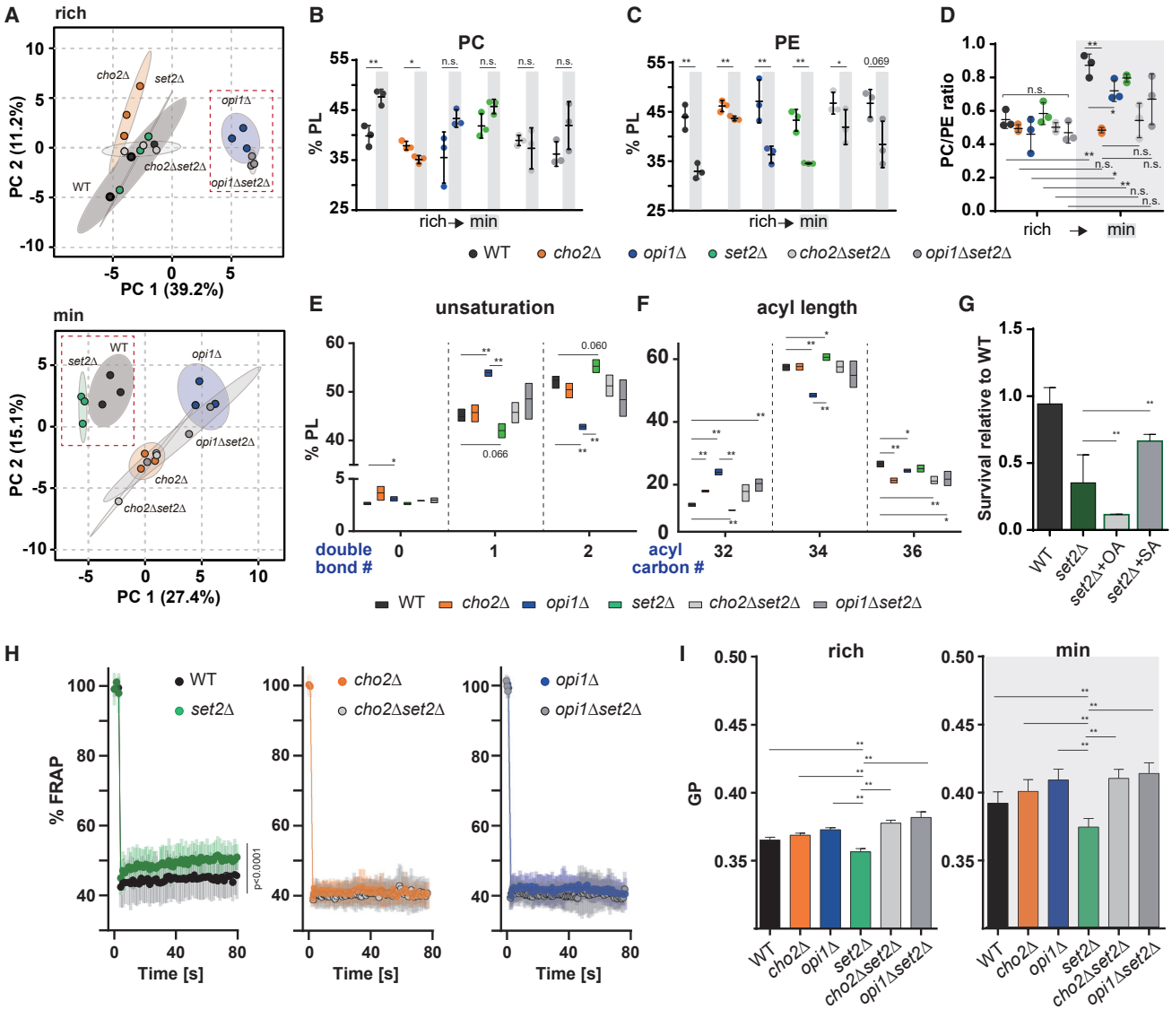

Figure 2. Phospholipid composition and membrane fluidity were influenced by nutrient starvation and H3K36 methylation

(A) PCA plots of phospholipid profiles in WT and indicated mutants in rich medium (top) and 12 h after starvation (bottom).

(B–F) PC (B), (C) PE, (D) PC/PE ratio, and relative amounts of phospholipid species calculated by the total number of double bonds (E; unsaturation) or carbons (F; acyl length) in two acyl chains. Data are expressed as percentages of total phospholipids and presented as mean ± SD (n = 3). *p < 0.05 and **p < 0.01; n.s., not significant.

(legend continued on next page)

et al., 2013), translational capacity (Laxman et al., 2013), and histone methylation events (Ye et al., 2017, 2019). Upon the switch, phosphatidylethanolamine (PE) methylation quickly consumes cellular SAM. It generates a low SAM signal, leading to activation of a network of enzymes responsible for methionine metabolism followed by concomitant decreases in histone methylation, particularly in H3K36 trimethylation (Ye et al., 2017). Within hours, both SAM levels and the amounts of methylated histones are partially restored (Ye et al., 2017, 2019). These observations led us to hypothesize that the crosstalk between phospholipid and histone methylation might mediate an adaptive response to nutrition deprivation.

We performed a prolonged culture to test cells' survivability in minimal medium as an outcome of adaptation to starvation. Unexpectedly, H3K36 methylation-deficient mutants, the mutant lacking H3K36 methyltransferase (*set2Δ*) and the point-mutation mutant (H3K36A), were very vulnerable to starvation and lost viability similarly at very fast rates (Figure 1B). Only fewer than 30% and 5% of these cells remained viable after 26 and 37 h, respectively (Figure 1B). This finding indicated that H3K36 methylation was essential for respiring cells to survive starvation. At 74 h, the PE methylation-deficient mutant *cho2Δ* and the *opi1Δ* mutant with hyperactive phospholipid synthesis exhibited markedly higher survival rates than wild-type (WT) (Figure 1B). Deletion of *CHO2* or *OPI1* rescued the survival rate of the *set2Δ* mutant to that of WT (Figure 1C). Therefore, the mutants adjusting phospholipid synthesis were epistatic to *set2Δ*, likely acting upstream of H3K36 methylation to provide a favorable mechanism for adapting starvation.

The phospholipid mutants enabled respiring cells to use different pathways for PC synthesis under starvation

We next investigated how the synthesis of phospholipids was modulated by the two phospholipid mutants *cho2Δ* and *opi1Δ*. Opi1 is a transcriptional repressor in the Henry regulatory circuit that controls phospholipid synthesis (Carman and Han, 2011; Henry et al., 2012). We show that Opi1 shuttles out of the nucleus to derepress phospholipid biosynthetic genes upon starvation (Ye et al., 2017). However, the export of Opi1 is not suppressed by exogenous inositol (Ye et al., 2017). This is different from the well-characterized mechanism of Opi1 translocation responding to inositol availability in glucose medium (Loewen et al., 2004; Young et al., 2010), underlying an unknown outcome of the Opi1-mediated mechanism in respiring cells. We showed previously that the synthesis of PC via PE methylation is defective in *cho2Δ* and hyperactive in *opi1Δ* cells by measuring SAM consumption (Ye et al., 2017). Here we further estimated the activity of the Kennedy pathway (also known as the CDP-choline pathway) for PC synthesis by measuring the consumption of three intermediary metabolites, choline, phosphocholine, and CDP-choline (Figure 1D). Upon the starvation switch, cellular levels of these metabolites were quickly consumed within 1 h in both WT and *cho2Δ* cells (Figure 1E). Notably, *cho2Δ* cells growing in rich medium contained higher amounts of CDP-choline, but that was decreased to the levels of WT cells upon starvation (Figure 1E). The greater consumption of CDP-choline confirmed that this pathway was more in demand in the *cho2Δ* mutant. In contrast, the amounts of phosphocholine and CDP-choline were decreased only marginally in *opi1Δ* cells (Figure 1E), suggesting that the Kennedy pathway in this mutant was not as active as in WT and *cho2Δ* cells. Thus, in respiring yeast cells, Opi1 functioned to regulate the synthesis of PC by altering the routes between PE methylation and the Kennedy pathway.

H3K36 trimethylation was increased in the phospholipid mutants under starvation

Unlike *cho2Δ*, which kept histones in the hypermethylation status within 2 h starvation (Ye et al., 2017), *opi1Δ* and WT cells exhibited a similar reduction pattern in the trimethylation of H3K4, H3K36, and H3K79 (Figure 1F). The trimethylated amounts of H3K36 (H3K36me3) were parallelly increased in *opi1Δ* cells compared with WT (Figure 1F) and remained higher in *cho2Δ* and *opi1Δ* cells even after 12 and 24 h (Figure S1). H3K36 trimethylation seemed to be a critical epigenetic mark linked to phospholipid metabolism for this adaptive transition. Blocking H3K79 methylation by *dot1Δ* did not affect the survivability, and *set2Δ* was sufficient to reduce the survival rate of the *dot1Δ* mutant (Figure 1G). H3K4 methylation deficiency in *set1Δ* also led to a reduced survival rate but did not exacerbate the survival rate of *set2Δ* (Figure 1G). We showed previously that blocking H3K4 methylation diminished H3K36 trimethylation, and blocking H3K36 methylation greatly increased H3K4 methylation (Ye et al., 2017). The interactive methylation between H3K4 and H3K36 might explain the observed survival phenotype.

PC/PE ratio and phospholipid acyl composition were affected by nutrient starvation and H3K36 methylation

To understand how phospholipids and H3K36 methylation influenced the adaptability to starvation, we performed quantitative mass spectrometry to analyze phospholipid composition in WT, *cho2Δ*, *opi1Δ*, *set2Δ*, *cho2Δset2Δ*, and *opi1Δset2Δ* cells before and 12 h after starvation. As revealed by principal-component analysis (PCA) (Figure 2A), *opi1Δ* and *opi1Δset2Δ* occupied a separate PCA space under the nutrient-rich condition, whereas WT and *set2Δ* became evidently separate from the long-surviving mutants 12 h after starvation in minimal medium, underlying a correlation between phospholipid composition and the survivability. Hierarchical clustering confirmed that the phospholipid mutants predominantly set cellular phospholipid compositions (Figure S2A). Phosphatidylinositol (PI) and phosphatidylserine (PS) were increased similarly upon starvation in all the strains (Figures S2B and

(G) Relative survival rates with 1 mM OA or SA.
(H) Normalized FRAP values of Mrh1-GFP in WT and indicated mutants. Data are represented as mean ± SD ($n \geq 14$).
(I) Membrane order state of spheroplasted cells assayed by the fluorescence spectral shift of Lauran. Data are expressed as GP values and presented as mean ± SD ($n = 6$). $^{**}p < 0.01$.
(J) Growth on rich medium with or without 1% Triton X-100 at 30°C or 37°C for 2 days.

S2C) and thus unlikely responsible for the differential adaptability to starvation.

We next focused on the most abundant phospholipids, PC and PE. WT cells exhibited increased PC (Figure 2B) and decreased PE levels (Figure 2C), with a more than 60% increase in PC/PE ratio after 12 h starvation (Figure 2D). This PC/PE ratio alteration was due to the methylation-mediated conversion of PE to PC, as blocking this process by *cho2Δ* largely prevented these alterations (Figures 2B, 2C, and 2D) during the switch. Despite the varying PC/PE ratios found in the 12 h starved cells (Figure 2D), only the *set2Δ* mutant showed a reduced survival rate 24 h after the switch (Figure 1B). We reasoned that phospholipid acyl composition might be altered along with the PC/PE ratio, and the ensuing head group and acyl composition could affect membrane functions. We analyzed phospholipid unsaturation and acyl length. The *set2Δ* mutant tended to have less mono-unsaturated but more di-unsaturated phospholipids (Figure 2E), and decreased C32 phospholipid levels in this mutant were accompanied by increases in C34 phospholipid species (Figure 2F). Such changes were opposite in the *opi1Δ* mutant and to a larger extent (Figures 2E and 2F). This sharp contrast illustrated a possibility that an overall increase in fatty acyl unsaturation or acyl length along with a decrease in PC/PE ratio might have challenged the survivability of *set2Δ*. Indeed, *opi1Δ* that normalized the aberrant acyl composition of *set2Δ* (Figure S2D) improved the survival rate (Figure 1C). The survival rates of *set2Δ* cells were also greatly reduced by oleic acid (OA; C18:1) supplemented in culture medium but slightly increased by stearic acid (SA; C18:0) (Figure 2G), suggesting that phospholipid unsaturation that agitates membrane fluidity might adversely affect the adaptability to starvation.

However, a comprehensive understanding of the effects of the increase in both unsaturation and acyl length along with PC/PE ratio in the *set2Δ* mutant is complicated by the fact that the acyl length of phospholipids affects membrane fluidity oppositely to unsaturation (van Meer et al., 2008). This might involve a mechanism compensatory to the skewed PC/PE ratio. A recent study shows an overall shift to short acyl chains in a PC-free yeast strain (Bao et al., 2021), highlighting an adaptive interplay between phospholipid class and acyl composition that may function to compensate for the biophysical property of cell membranes (Ballweg et al., 2020).

Loss of H3K36 methylation increased membrane fluidity and sensitivity to a membrane detergent

We examined if loss of H3K36 methylation might disrupt membrane functions such as membrane fluidity and permeability because of the resulting alterations in phospholipid composition. First, we assessed membrane fluidity by measuring the lateral diffusion rate of a membrane protein (Mrh1-GFP) with the fluorescence recovery after photobleaching (FRAP) assay (Ruiz et al., 2018; Singh et al., 2017). Strikingly, the relative fluorescence gain of *set2Δ* was significantly greater and faster than that of WT cells (Figures 2H and S2E). The difference in fluorescence recovery was not due to the differential expression of the reporter protein (Figure S2F). In addition, the diffusion of Mrh1-GFP was immobilized by deletion of *CHO2* or *OPI1* (Figure 2H), suggesting the aberrant phospholipid composition in the *set2Δ* mutant was likely responsible for the increase in membrane fluidity.

Next, we examined the lipid packing state of spheroplasted cells by measuring the fluorescence spectral shift of Lauran, a lipophilic dye used to report membrane surface order (Kaiser et al., 2011; Toulmay and Prinz, 2013). The membrane surface order state was represented as a general polarization (GP) value. Loss of H3K36 methylation in *set2Δ* resulted in lower GP values (Figure 2I), indicating the less ordered and more fluidic cell membrane state. Notably, starvation and the phospholipid mutants increased GP values, indicating that a more rigid membrane was favored under starvation. On this notion, the overall increase in unsaturated phospholipids (Figure 2E) and supplementation of OA (Figure 2G) might adversely affect the rigidity of the membrane state, exacerbating the survival rate of H3K36 methylation-deficient cells.

Last, we assessed membrane integrity by growing cells on rich medium with 1% Triton X-100 to test membrane resistance to a detergent (Schuck et al., 2003; Singh, 2016). We found that only the mutants *set2Δ* and H3K36A were sensitive to the detergent. Their growth in the presence of Triton X-100 was retarded at 30°C and became exceedingly slow at 37°C (Figures 2J and S2H). This growth defect marked impaired membrane integrity associated with loss of H3K36 methylation. We reasoned that the increases in unsaturated phospholipids were accountable for this membrane defect. We purposely altered acyl composition by pre-growth of cells with fatty acids (Lou et al., 2018). The rescue effect executed by the phospholipid mutants was abolished by OA (Figures 2J and S2H) but not by SA (Figure S2G), suggesting that membrane defects associated with H3K36 methylation deficiency were likely due to increased incorporation of OA into membrane phospholipids.

The gene regulation role of H3K36 methylation was unimportant for phospholipid synthesis

To understand how the loss of H3K36 methylation led to the abnormal phospholipid composition, we reasoned if the transcriptional control of phospholipid biosynthetic genes was governed by H3K36 methylation. First, we examined if H3K36me3 enrichment was associated with transcriptional regulation of phospholipid biosynthetic genes. On the basis of our previous sequencing data (Ye et al., 2019), the H3K36me3 mark is enriched at gene bodies (Figure S3A) and greatly reduced upon starvation (Figures S3A and S3B). The boxplot illustrated a negative correlation between H3K36me3 and gene expression (Figure S3B). For example, the set of methionine metabolism genes (MET) that are the most upregulated is associated with decreased H3K36me3 enrichment (Figure S3B). The transcription of and H3K36me3 enrichment in phospholipid biosynthetic genes changed only moderately upon starvation, exhibiting an inverse correlation trend (Figure 3A). If H3K36me3 were repressive to transcription of these genes, their mRNA transcript levels would be elevated in H3K36 methylation-deficient mutants. We performed additional RNA sequencing (RNA-seq) and found that mRNA levels of the phospholipid biosynthetic genes were not overtly increased upon the loss of H3K36 methylation (Figure 3B). For example, the transcription of *INO1* and *OPI3* was upregulated with reduced H3K36me3

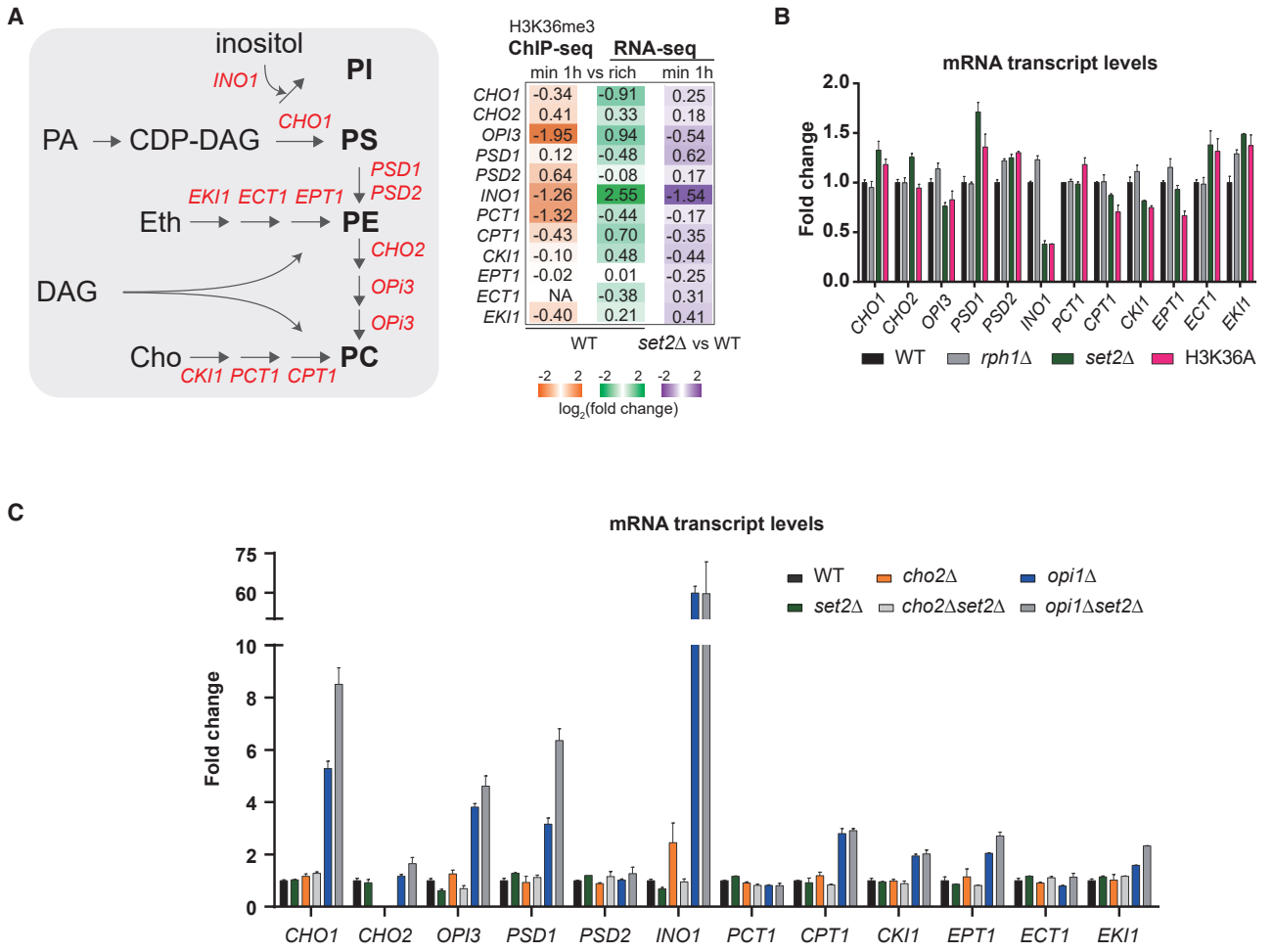

Figure 3. The gene regulation role of H3K36 methylation was unimportant for the expression of phospholipid genes

(A) Left: pathway and genes for phospholipid biosynthesis. Right: relative fold change of H3K36me3 enrichment and mRNA transcript levels for phospholipid genes.

(B and C) Relative mRNA transcript levels. Data were calculated from the FPKM (fragments per kilobase of transcript per million mapped fragments) values of RNA-seq data.

enrichment, but their expression was decreased in the *set2Δ* mutant (Figures 3A and 3B). In fact, an overall change of transcription was not observed at the whole-transcriptome level by blocking either methylation or demethylation of H3K36 (Figure S3C). Our findings thus argued against that H3K36 methylation was a driving regulator modulating the transcription of phospholipid genes during this adaptation process.

We further profiled the transcriptomes of the double-deletion mutants *cho2Δset2Δ* and *opi1Δset2Δ* 1 h after starvation. Hierarchical clustering revealed that loss of H3K36 methylation partitioned the transcriptome datasets into two major sub-clusters (Figure S3D), indicating that *set2Δ* was epistatic to the phospholipid mutants with respect to transcriptional alterations under starvation. Also, *opi1Δ* influenced the transcriptome of *set2Δ* much more than *cho2Δ* as to the number of differentially expressed genes (Figure S3E), probably because Opi1 is a transcription factor. However, loss of H3K36 methylation had a neglectable effect on the expression of phospholipid biosynthetic genes even in the phospholipid mutants (Figure 3C), substantiating that the transcriptional role of H3K36 methylation was not important in modulating the phospholipid composition of *set2Δ*.

RNA-seq analysis revealed an increase in the expression of nutrient transporter genes in H3K36 methylation-deficient mutants

The Gene Ontology (GO) analysis revealed two top categories, integral component of membrane and transmembrane transport (Figure 4A; Table S1), pointing to a potential solute transport defect in the H3K36 methylation-deficient mutants. We manually went through the lists of genes in the *set2Δ* and H3K36A mutants differentially expressed from WT before and after the starvation and found a total of 139 membrane-related genes (Table S2). We curated three groups with 83 genes in transporters, 15 in iron metabolism, and 41 in other membrane proteins (Table S2; Figure 4B). Many of these genes function in nutrient uptake,

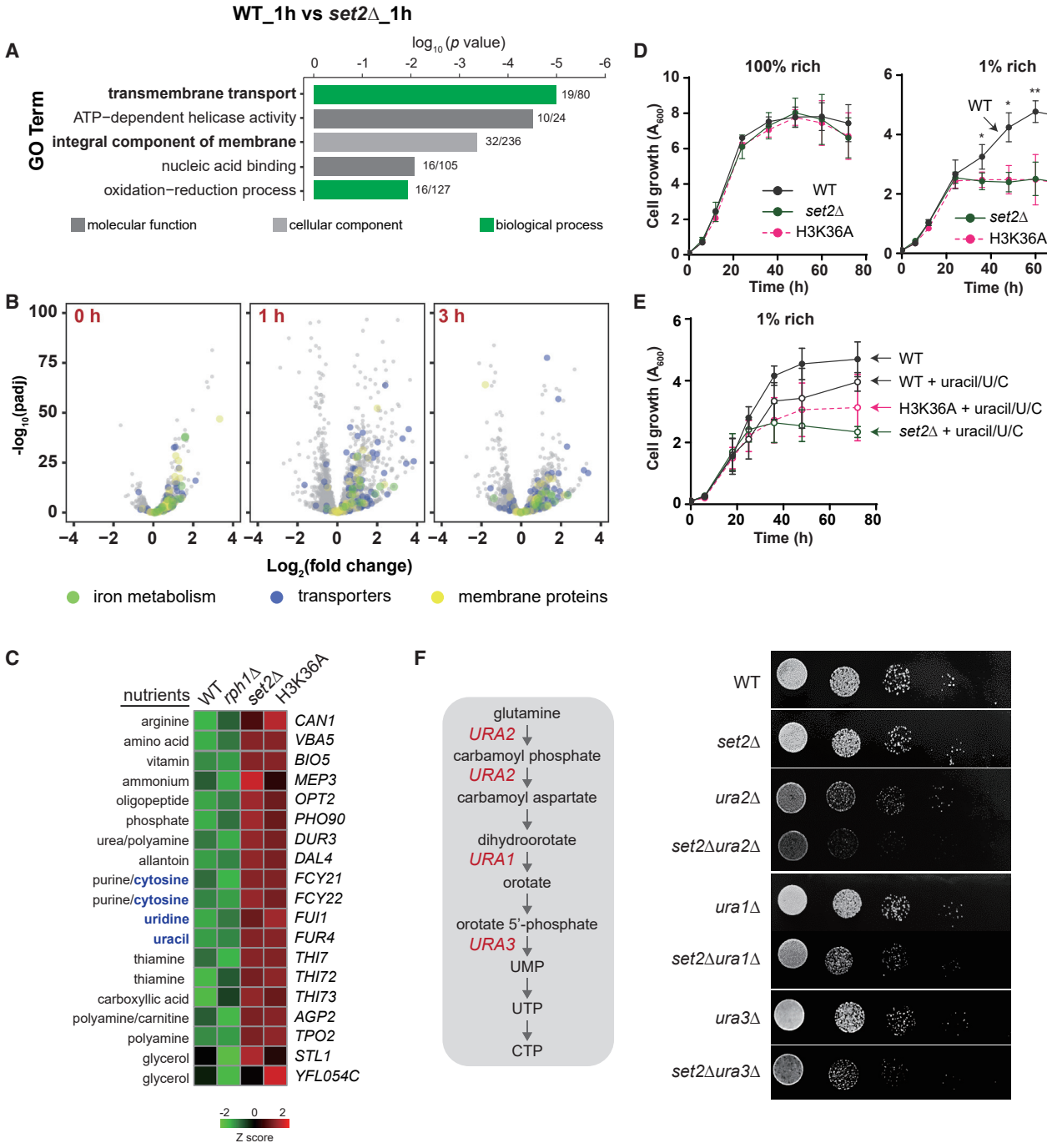

Figure 4. The optimal growth of H3K36 methylation-deficient mutants depended on the quantity of nutrients and a functional pathway for pyrimidine *de novo* synthesis

(A) GO term analysis of differentially expressed genes under 1 h starvation.

(B) Volcano plots of RNA-seq data depicting differentially expressed genes.

(C) Heatmap of differentially expressed transporters.

(D and E) Growth curves in 100%, 1% rich medium, or 1% rich medium with a mixture of uracil, uridine (U), and cytidine (C). Data are represented as mean ± SD (n = 3). *p < 0.05 and **p < 0.01.

(F) Left: pyrimidine de novo synthesis pathway. Right: growth on rich medium after incubation at 30°C for 2 days.

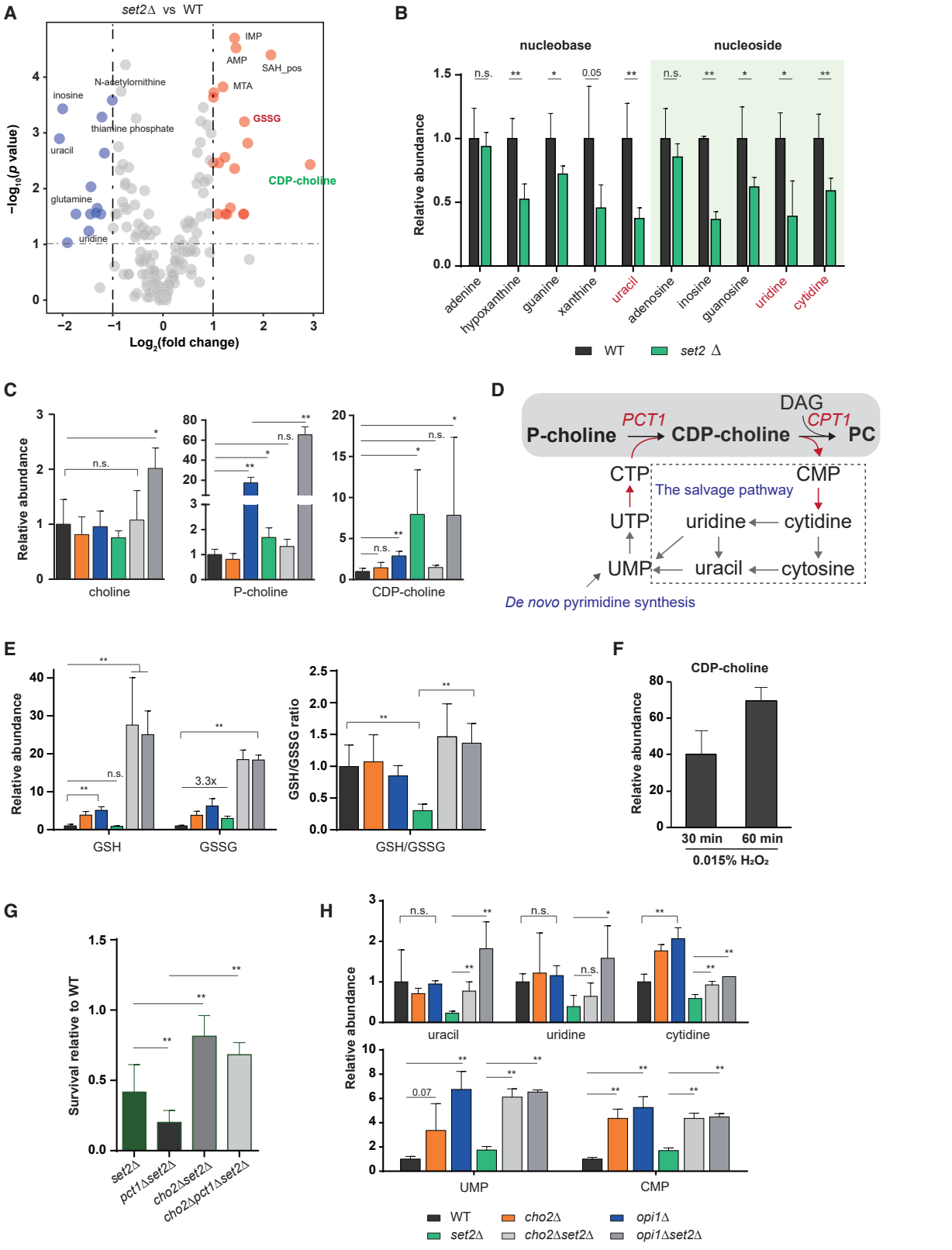

(legend on next page)

iron use, ion transport, and lipid transport (Figures 4C and S3G). Most of them were transcriptionally upregulated in the mutants blocking H3K36 methylation, and the extent of upregulation became more pronounced under starvation (Table S2; Figure 4B). However, the starvation condition alone did not cause a prominent upregulation, with only 49 up- and 40 down-regulated in WT cells (Figure S3H). An average increase in H3K36me3 amounts across these gene bodies was observed 1 h after the switch (Figure S3F) (Ye et al., 2019). Most of these genes were not transcriptionally repressed in the mutants bearing hyper-methylated H3K36, such as the H3K36 demethylase mutant *rph1Δ* and a high SAM content mutant *cho2Δ* (Table S2; Figure S3H). These observations confounded a consensus role of H3K36 methylation in transcriptional control of these membrane genes.

Because the action of membrane proteins such as transporters embedded in cellular membranes was crucially dependent on phospholipid composition (van Meer et al., 2008; Zhang and Rock, 2008), the phospholipid abnormalities resulting from loss of H3K36 methylation may perturb transporter activities, making the mutant cells hypersensitive to the quantity of nutrients. To test this idea, we measured cell growth in a low amount of nutrients by diluting rich medium with minimal medium to 1%. The growth curves of *set2Δ* and H3K36A cells similarly plateaued at lower absorbance readings in this low-nutrient medium (Figure 4D), indicating that loss of H3K36 methylation conferred growth sensitivity to the quantity of nutrients.

Loss of H3K36 methylation exhibited metabolic deficiency in pyrimidine metabolism

Interestingly, many genes encoding uptake transporters for pyrimidine metabolites (*FCY21*, *FCY22*, *FUI1*, and *FUR4*) were transcriptionally upregulated in the *set2Δ* and H3K36A mutants (Figure 4C), underlying a metabolic need for pyrimidine metabolites. However, adding a mixture of uracil, uridine, and cytidine did not affect the growth of these mutant cells in the 1% rich medium (Figure 4E). In stark contrast, deletion of *URA2*, *URA1*, or *URA3* to disrupt *de novo* synthesis of pyrimidines was sufficient to retard the growth of *set2Δ* (Figure 4F). This synthetic sickness phenotype revealed growth dependence of H3K36 methylation deficiency on pyrimidine *de novo* synthesis.

To examine pyrimidine metabolism and potential metabolic perturbations in the H3K36 methylation-deficient mutants, we performed targeted metabolomics to profile relative abundances of cellular metabolites for surviving cells starved for 12 h. The volcano plot revealed 31 metabolites with abundances differential significantly in the starved WT and *set2Δ* cells (Figure 5A). Surprisingly, 12 were purine and pyrimidine metabolites (Table S3), including inosine, uracil, and uridine, whose levels were reduced to less than 50% in *set2Δ* cells compared with WT (Figure 5A). Except for adenine and adenosine, the amounts of nucleobase and nucleoside were all reduced in the *set2Δ* cells (Figure 5B). These findings featured an imbalanced purine and pyrimidine metabolism that might be unfavorable under starvation.

H3K36 methylation deficiency led to an oxidation-responsive inhibition of the CDP-choline pathway for PC synthesis, forming a pyrimidine cache that diminished pyrimidine recycling

Intriguingly, blocking H3K36 methylation led to about an 8-fold increase in a pyrimidine-containing metabolite, CDP-choline (Figures 5A and 5C), an active form of choline that is condensed with diacylglycerol (DAG) to produce PC in the last step of the Kennedy pathway (Figure 5D). We found that DAG levels were not affected by H3K36 methylation (Figure S4A). In contrast, the accumulation of CDP-choline was accompanied by an increase in oxidized glutathione (GSSG) and a profound drop in GSH/GSSG ratio in the starved *set2Δ* cells (Figure 5E), suggesting that the oxidative environment might be inhibitory to the final condensation step of PC synthesis. Consistent with this, hydrogen peroxide (H_2O_2)-induced oxidative stress led to sharp increases in CDP-choline (Figure 5F). Because PC and PE acyl composition can be affected by different use of the two major PC biosynthesis pathways (Boumann et al., 2003, 2004; DeLong et al., 1999), the oxidative inhibition of the CDP-choline pathway likely contributed to the aberrant acyl composition of H3K36 methylation deficiency (Figures 2E and 2F).

The accumulation of CDP-choline cached a pool of pyrimidine metabolites unattainable temporarily, so we named this phenomenon pyrimidine cache hereafter. This pyrimidine cache probably disrupted pyrimidine homeostasis because it impeded the recycling of cytidylate that feeds into the salvage pathway (Figure 5D). Consistent with this, the starved *set2Δ* cells contained lower amounts of pyrimidine metabolites such as uracil, uridine, and cytidine (Figure 5B) and exhibited growth dependency on the *de novo* pathway for pyrimidine synthesis (Figure 4F). In addition, blocking the turnover of CTP via the CDP-choline pathway by deletion of *PCT1* reduced the survival

Figure 5. H3K36 methylation licensed redox-sensitive synthesis of PC via the CDP-choline pathway whose activity affected pyrimidine homeostasis

(A) Volcano plot of targeted metabolomics in the 12 h starved WT and *set2Δ* cells.

(B and C) Relative abundances of nucleobases and nucleosides (B) and (C) choline, phosphocholine, and CDP-choline in the 12 h starved cells. Data are presented as mean ± SD (n = 4). *$p < 0.05$ and **$p < 0.01$; n.s., not significant.

(D) Schematic of a metabolic intersection between PC synthesis and pyrimidine metabolism.

(E) Relative abundances of GSH, GSSG, and GSH/GSSG ratio in indicated cells 12 h after the switch to minimal medium. Data are presented as mean ± SD (n = 4). *$p < 0.05$ and **$p < 0.01$; n.s., not significant.

(F) Relative abundances of CDP-choline in WT cells after H_2O_2 treatment. Data are presented as mean ± SD (n = 3).

(G) Relative survival rates after 24 h starvation. Data are presented as mean ± SD ($n \geq 3$). **$p < 0.01$.

(H) Relative abundances of uracil, uridine, cytidine, UMP, and CMP in the 12 h starved cells. Data are presented as mean ± SD (n = 4). *$p < 0.05$ and **$p < 0.01$; n.s., not significant.

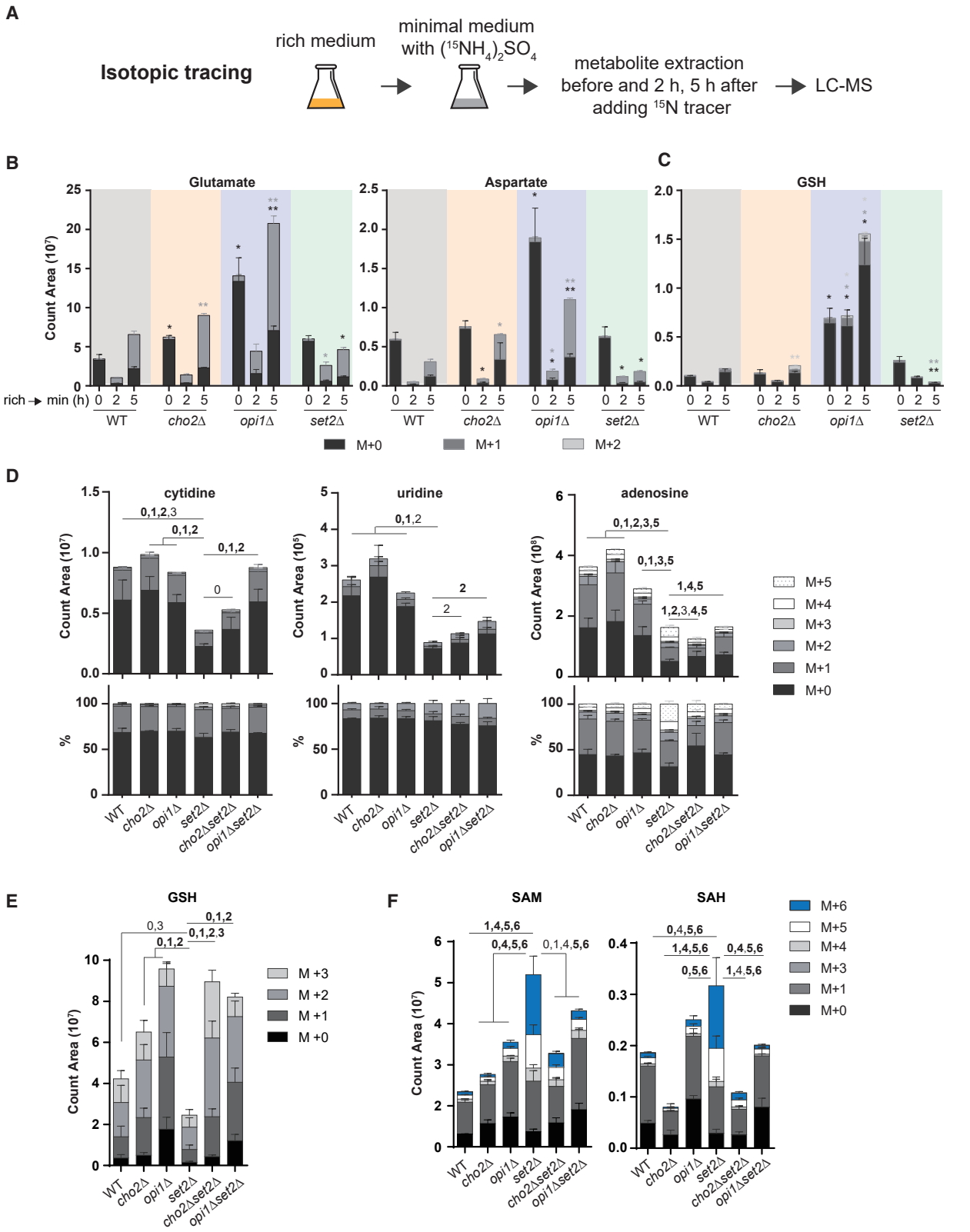

(legend on next page)

rate of *set2Δ* (Figure 5G), suggesting that oxidative inhibition of PC synthesis and the resulting accumulation of CDP-choline contributed to the survival defect. Nonetheless, deletion of *CHO2* improved the survival rate of *pct1Δset2Δ* (Figure 5G), even with two major routes for PC synthesis being defective, underlying additional pro-survival mechanisms.

We found that the decreases in uracil, uridine, and cytidine in the *set2Δ* mutant were restored by deletion of *CHO2* and *OPI1* (Figure 5H), coincident with the improved adaptability in the *cho2Δset2Δ* and *opi1Δset2Δ* mutants (Figure 1C). These observations confirmed that maintaining pyrimidine homeostasis is critical for survival under starvation. Interestingly, the pyrimidine cache formed in *set2Δ* was resolved only by the phospholipid mutant *cho2Δ*, not by *opi1Δ* (Figure 5C). Notably, phosphocholine levels in the *set2Δ* mutant were increased by *opi1Δ* (Figure 5C). Thus, resolving the pyrimidine cache was unnecessary for the phospholipid mutants to rescue pyrimidine deficiency. Because the levels of pyrimidine nucleotides were elevated by *cho2Δ* and *opi1Δ* (Figure 4H), another possible explanation was that the biosynthesis process might be activated to replenish pyrimidine metabolites.

Rewiring phospholipid synthesis necessitated metabolic coordination to promote purine and pyrimidine biosynthesis

To understand how the phospholipid mutants influenced metabolism under starvation, we performed metabolomics clustering analysis of the 12 h starved cells. Unlike the clustering pattern of phospholipid composition under starvation, the metabolite profiles of the two phospholipid mutants and the two double mutants were clustered together on their own (Figure S5A). The fact that the relative abundances of many metabolites in *cho2Δ* and *opi1Δ* cells differed from those in WT and *set2Δ* cells (Figure S5A) indicated that the rewiring of PC synthesis could potently alter metabolic fates. Moreover, the deletion of *SET2* in *cho2Δ* and *opi1Δ* created an outstanding cluster, bolstering metabolic connection between phospholipid metabolism and H3K36 methylation (Figure S5A). In particular, *cho2Δ* and *opi1Δ* led to substantial increases in intermediary metabolites in gluconeogenesis (Figure S5B), the pentose phosphate pathway (PPP) (Figure S5C), and the tricarboxylic acid (TCA) cycle (Figure S5E). Because the levels of many purine and pyrimidine metabolites were concomitantly increased in the phospholipid mutants (Figures S4B and S4C), regulation of PC synthesis might enable powerful reprogramming of metabolism under starvation to supply ribose and nitrogenous base for making nucleotides.

We next performed an isotopic tracing experiment using ^{15}N-ammonium sulfate to examine the metabolic flux of nitrogenous metabolites (Figure 6A). We found that cellular glutamate and aspartate depleted upon starvation were replenished within 5 h by active re-synthesis (Figure 6B). Compared with WT cells, *cho2Δ* and *opi1Δ* cells contained higher amounts of ^{15}N-incorporated glutamate and aspartate, whereas the unlabeled levels were reduced significantly in *set2Δ* cells (Figure 6B). Therefore, rewiring the synthesis of PC and H3K36 methylation deficiency had opposite effects on the cataplerotic production of glutamate and aspartate under starvation. Because ^{15}N was incorporated into only small fractions of cytidine, uridine, and adenosine within 5 h starvation (Figure S6A), we performed another 12 h tracing experiment. The amino acid precursors glutamine and aspartate for purine and pyrimidine synthesis became mostly heavily labeled after 12 h (Figure S6B). Similarly, the phospholipid mutants and the *set2Δ* mutant opposed different influences on the production of these amino acids (Figure S6A), and the phospholipid mutants were able to restore this deficiency in the *set2Δ* mutant (Figure S6B). Followed by increases in these labeled amino acids, ~35% cytidine, ~25% uridine, and more than 50% adenosine were ^{15}N-incorporated (Figure 6D), suggesting that purines were more actively synthesized *de novo* than pyrimidines under starvation. In addition, we found greater reductions in unlabeled cytidine and uridine levels in *set2Δ* cells (Figure 6D), consistent with poor pyrimidine recycling in the presence of the pyrimidine cache. Nearly all labeled species of cytidine and uridine were comparatively lower in the *set2Δ* mutant (Figure 6D), confirming defective pyrimidine *de novo* synthesis. To our surprise, the amounts of fully labeled adenosine (M+5) were increased moderately in *set2Δ* cells (Figure 6D). Such imbalanced purine production over pyrimidine was in part or fully restored by the phospholipid mutants (Figure 6D). Overall, these tracing experiments suggested that rewiring the synthesis of phospholipids activated a network of metabolic programs to generate precursor metabolites, the availability of which might limit the production of pyrimidines.

H3K36 methylation deficiency restrained SAM turnover for GSH production

Because the Kennedy pathway for PC synthesis was sensitive to oxidative stress and its inhibition disrupted pyrimidine metabolism, we next investigated if the methyl group sink function of H3K36 contributed to the control of redox homeostasis under starvation. We found that GSH levels were augmented in the phospholipid mutants whereas GSH/GSSG ratio was reduced in the starved *set2Δ* cells, and such reduction in *set2Δ* could be restored by *cho2Δ* and *opi1Δ* (Figure 5E). The amounts of unlabeled and labeled GSH were markedly increased in *opi1Δ* cells after 5 h starvation as shown in the tracing experiment, while the labeled GSH level was only slightly but significantly increased in *cho2Δ* cells (Figure 6C). The 12 h tracing experiment confirmed increased GSH production by *cho2Δ* and *opi1Δ* (Figure 6E). In contrast, unlabeled and labeled

Figure 6. Rewiring the synthesis of phospholipids facilitated the cataplerotic synthesis of precursor amino acids for nucleotide production and GSH production

(A) Schematic of the experiment design for isotopic tracing using $(^{15}NH_4)_2SO_4$.

(B and C) Levels of ^{15}N-labeled (gray) and unlabeled (dark) glutamate, aspartate, and GSH in the 5 h isotopic tracing experiment. Data are presented as mean ± SD (n = 3). p values in gray or dark for labeled and unlabeled metabolites; *p < 0.05 and **p < 0.01.

(D–F) Levels of ^{15}N-labeled and unlabeled cytidine, uridine, adenosine (D), (E) GSH, (F) SAM, and SAH after 12 h tracing. Data are presented as mean ± SD (n = 6). Number X designates statistical significance (p < 0.05) of a particular metabolite with X mass shift; number in boldface type designates p < 0.01.

GSH levels gradually decreased in *set2Δ* cells (Figure 6C), further corroborated by the 12 h tracing experiment (Figure 6E). Although GSH production was defective in the absence of H3K36 methylation, the amounts of fully labeled SAM (M+6) and SAH (M+6) were increased more than 10-fold (Figure 6F). The levels of SAM and SAH containing fully labeled adenosine (M+5) were also greatly increased in the starved *set2Δ* cells (Figure 6F). Therefore, the GSH deficiency of *set2Δ* was likely due to being unable to turn over newly synthesized SAM through this histone methyl sink in the nucleus.

Alternative pathways for PC biosynthesis adopted distinct metabolic programs for methionine metabolism

Interestingly, we found that phospholipid mutants *cho2Δ* and *opi1Δ* were both able to prevent SAM and SAH accumulation in the *set2Δ* cells starved for 12 h (Figure 6F), suggesting that rewiring the synthesis of phospholipids could facilitate SAM turnover for GSH production. This raises a corollary conundrum: why were the cells with a defect in the major methyl sink of PE methylation able to promote GSH production under starvation? We postulated that SAM turnover through the phospholipid methyl sink provides an immediate antioxidant source for oxidative defense. The following SAM depletion activates the transcriptional program for methionine metabolism and the demethylation of histones to prepare for the second line of oxidative defense (Ye and Tu, 2018). To test this, we examined protein levels of metabolic enzymes in methionine pathways (Figure 7A). As shown in Figure 7B, the protein levels of enzymes in the sulfate assimilation pathway were sharply increased after 2 h starvation in WT and *set2Δ* cells, which were repressed by exogenous methionine. However, the methionine cycle and the transsulfuration pathway were not as responsive to starvation, as the respective enzyme abundances remained largely unchanged (except for Sam1 in *opi1Δ* and Str3). The sulfate assimilation pathway enzymes were very abundant in the *cho2Δ* mutant even under the nutrient-replete condition. Their expression was not altered upon starvation, suggesting that this pathway was hyperactive when PE methylation was deficient. In contrast, the activation of the expression of these enzymes was defective in *opi1Δ* cells (Figure 7B). The methionine cycle enzymes were also altered in the *opi1Δ* mutant. In particular, SAM synthetase Sam1 was repressed while the other SAM synthetase Sam2 increased, and SAH hydrolase Sah1 protein was increased profoundly (Figure 7B). Such changes probably activated the methionine cycle in the *opi1Δ* mutant. These findings explicated an example of metabolic plasticity in which use of alternative pathways for PC synthesis was tied to a unique metabolic program of sulfur acquisition. This intrinsic connectivity of PC synthesis to sulfur metabolism may empower metabolic reprogramming under starvation. Consistent with this idea, deletion of *MET6* reduced the survival rate of the *opi1Δset2Δ* mutant (Figure 7C), suggesting that the active methionine cycle was required for *opi1Δ* to restore the survival deficiency of the *set2Δ* mutant. Notably, the survival rate of the *cho2Δset2Δ* mutant was increased by 50% when *MET6* was additionally deleted (Figure 7C). Future investigation is warranted to address how such regulation of methionine metabolism ensures pyrimidine and redox homeostasis under starvation.

DISCUSSION

It remains largely elusive how membrane lipids integrate environmental cues for regulation at the interface of extra- and intracellular environments. In this study, we uncover that the synthesis of phospholipids can necessitate metabolic coordination to meet environmental requirements. We demonstrate an adaptive mechanism by which reciprocal regulation of PC synthesis and H3K36 methylation operates a homeostatic control of nucleotide metabolism in the redox environment.

Our model proposes that PE methylation can translate nutrient insufficiency into a low SAM signal under starvation (Ye et al., 2017). This metabolic information is relayed, at least in part, through a PP2A-governed demethylation event on the histone H3K36 in the nucleus (Ye et al., 2019). While re-methylation of H3K36 facilitates GSH production for redox balancing, the CDP-choline pathway for PC synthesis proceeds (Figure 7D). It is worth noting that choline phosphate cytidylyltransferase, the rate-limiting enzyme of the CDP-choline pathway, is intra-nuclear in yeast, fly, and mammalian cells, whose activation is dependent on the recruitment to the inner nuclear membrane (Haider et al., 2018). Metabolic status in the nucleus influenced by histone methylation thus may modulate the synthesis of phospholipids in the vicinity of the nuclear membrane territory (Romanauska and Kohler, 2018; Romanauska and Köhler, 2021).

Our findings unveil a novel idea that promoting phospholipid synthesis can be exploited as a cellular strategy to resist stress. We observed that starvation and rewiring PC synthesis resulted in many metabolic changes related to mitochondrial metabolism. Because mitochondrial membrane lipids are susceptible to the altered PC/PE ratio and fatty acyl composition (Budin et al., 2018; Renne et al., 2021), mitochondrial function and metabolism may be readily affected by alterations in phospholipid composition. For example, the starting material for the TCA cycle, acetyl-CoA, was elevated in the phospholipid mutants and further increased by *set2Δ* (Figure S5E). Concomitant with the increase in acetyl-CoA, we found increases in acetylated histones such as H3K9ac and H3K56ac in the *opi1Δ* mutant (Figure 1F). These findings underscored a possible mechanism by which lipid metabolism is linked to metabolic adaptation via acetylation regulation of histones. We propose that membrane-metabolism coordination represents an efficient means to ensure environmental adaptation.

Among various cellular functions of H3K36 methylation, such as these in transcription (Carrozza et al., 2005; Lee et al., 2013; Sen et al., 2015; Wen et al., 2014; Xu et al., 2009), DNA repair (Fnu et al., 2011; Pryde et al., 2009), and mRNA splicing (Sorenson et al., 2016), we characterized an unforeseen metabolic function for H3K36 methylation serving as a methyl group sink in the nucleus (Ye et al., 2017, 2019; Ye and Tu, 2018). An exciting discovery in this study is that H3K36 methylation is very sensitive to nutrient status and required for survivability under starvation. This resonates with the critical roles of H3K36 methylation in nutrient stress response (McDaniel et al., 2017) and longevity (Pu et al., 2015; Sen et al., 2015) and

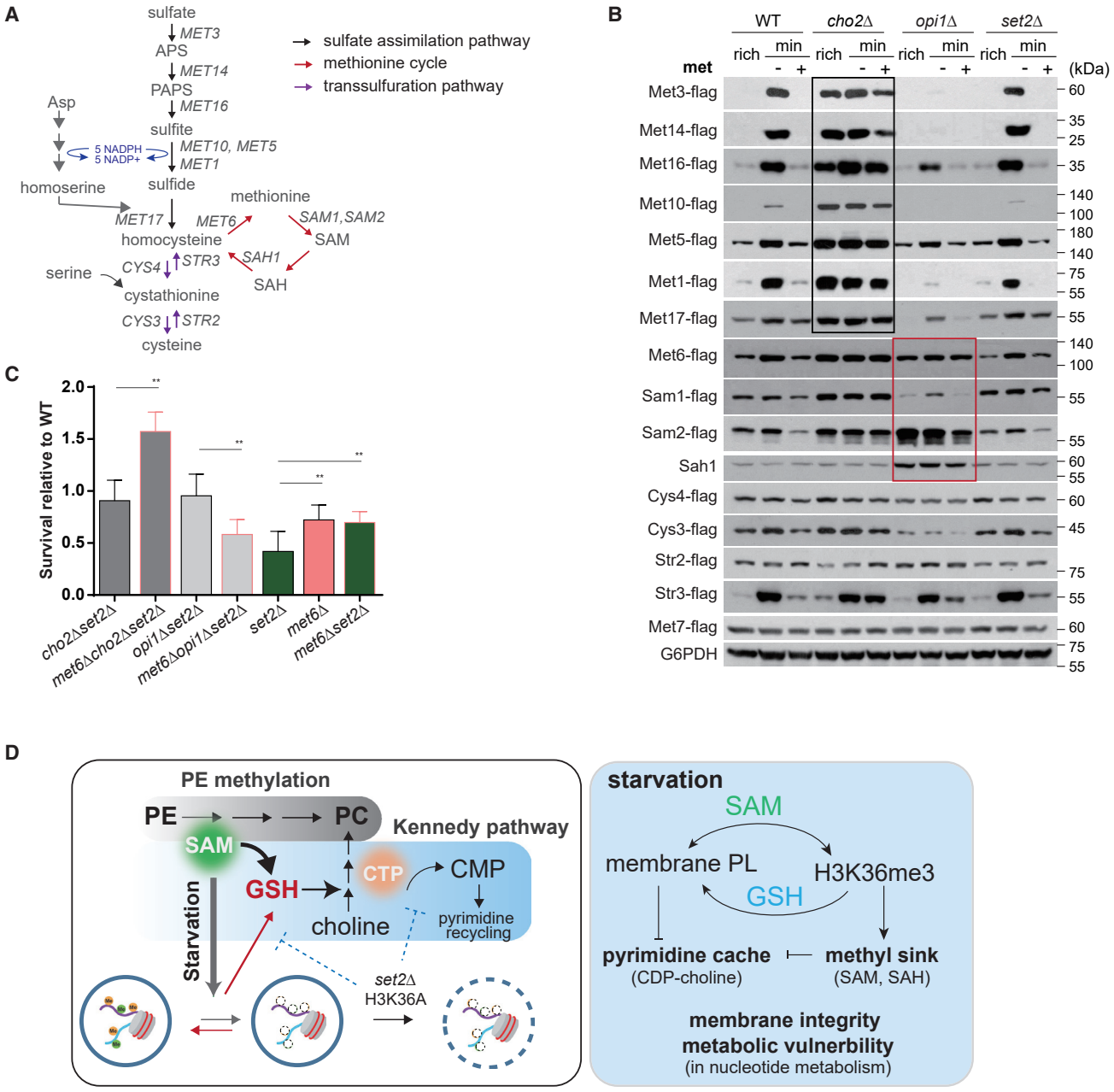

Figure 7. Alternative pathways for PC biosynthesis activated distinct metabolic programs for methionine metabolism

(A) Pathways for methionine metabolism.

(B) Protein abundances of methionine metabolic enzymes. Data are representative of three independent validations.

(C) Relative survival after 24 h starvation. Data are presented as mean ± SD ($n \geq 3$). **$p < 0.01$.

(D) Mechanistic model underlying functional crosstalk between PC synthesis and H3K36 methylation for adapting nutrient starvation.

sheds light on a new perspective to dissecting information carried by this epigenetic mark.

Limitations of the study

Here we provide evidence that the phospholipid mutants of rewiring PC synthesis adjust phospholipid head group and acyl composition in accordance with metabolic reprogramming of various pathways, including the TCA cycle and nucleotide metabolism. Although the membrane defects resulting from H3K36 methylation deficiency are rescued by the mutants normalizing the aberrant phospholipid composition, the attributing membrane systems and organelles sensitive to such lipid alterations and responsible for adaptability remain elusive. Furthermore, how rewiring PC synthesis exerts regulation of

methionine metabolism to ensure pyrimidine and redox homeostasis awaits further investigation.

STAR★METHODS

Detailed methods are provided in the online version of this paper and include the following:

- KEY RESOURCES TABLE
- RESOURCE AVAILABILITY
  - Lead contact
  - Materials availability
  - Data and code availability
- EXPERIMENTAL MODEL AND SUBJECT DETAILS
- METHOD DETAILS
  - Determination of survival rates
  - Determination of growth rates of yeast cells by absorbance at 600 nm or spotting assay
  - Lipid extraction and quantification
  - Determination of plasma membrane fluidity by fluorescence recovery after photo bleaching (FRAP) measurement
  - Determination of membrane order with Laurdan
  - RNA-seq analysis
  - Metabolite extraction and quantitation
  - Metabolic flux analysis using ^{15}N ammonium sulfate
  - Whole yeast cell extracts preparation and western blotting
- QUANTIFICATION AND STATISTICAL ANALYSIS
  - Hierarchical clustering and heat maps
  - Statistical analysis

SUPPLEMENTAL INFORMATION

Supplemental information can be found online at https://doi.org/10.1016/j.celrep.2022.110672.

ACKNOWLEDGMENTS

This work was supported by grants from the National Natural Science Foundation China (92057102), the Fundamental Research Funds for the Central Universities (2-2050205-20-489), the Fundamental Research Funds for Zhejiang Provincial Colleges & Universities, a research fund from Zhejiang Provincial Key Laboratory for Cancer Molecular Cell Biology, the startup fund from the Life Sciences Institute of Zhejiang University, and the 1000 Talents Program for Young Scholars to C.Y.

AUTHOR CONTRIBUTIONS

C.Y. conceived this study and wrote the manuscript. W.F. and Y.Z. performed all the experiments except these noted. S.Y. performed lipid analysis using mass spectrometry. X.T. helped with strain construction and western blotting experiments.

DECLARATION OF INTERESTS

The authors declare no competing interests.

Received: September 13, 2021
Revised: January 14, 2022
Accepted: March 22, 2022
Published: April 12, 2022

REFERENCES

Ballweg, S., Sezgin, E., Doktorova, M., Covino, R., Reinhard, J., Wunnicke, D., Hanelt, I., Levental, I., Hummer, G., and Ernst, R. (2020). Regulation of lipid saturation without sensing membrane fluidity. Nat. Commun. *11*, 756.

Bao, X., Koorengevel, M.C., Groot Koerkamp, M.J.A., Homavar, A., Weijn, A., Crielaard, S., Renne, M.F., Lorent, J.H., Geerts, W.J., Surma, M.A., et al. (2021). Shortening of membrane lipid acyl chains compensates for phosphatidylcholine deficiency in choline-auxotroph yeast. EMBO J. *40*, e107966.

Boumann, H.A., Chin, P.T., Heck, A.J., De Kruijff, B., and De Kroon, A.I. (2004). The yeast phospholipid N-methyltransferases catalyzing the synthesis of phosphatidylcholine preferentially convert di-C16:1 substrates both in vivo and in vitro. J. Biol. Chem. *279*, 40314–40319.

Boumann, H.A., Damen, M.J., Versluis, C., Heck, A.J., de Kruijff, B., and de Kroon, A.I. (2003). The two biosynthetic routes leading to phosphatidylcholine in yeast produce different sets of molecular species. Evidence for lipid remodeling. Biochemistry *42*, 3054–3059.

Budin, I., de Rond, T., Chen, Y., Chan, L.J.G., Petzold, C.J., and Keasling, J.D. (2018). Viscous control of cellular respiration by membrane lipid composition. Science *362*, 1186–1189.

Cai, L., Sutter, B.M., Li, B., and Tu, B.P. (2011). Acetyl-CoA induces cell growth and proliferation by promoting the acetylation of histones at growth genes. Mol. Cell *42*, 426–437.

Carman, G.M., and Han, G.S. (2011). Regulation of phospholipid synthesis in the yeast Saccharomyces cerevisiae. Annu. Rev. Biochem. *80*, 859–883.

Carrozza, M.J., Li, B., Florens, L., Suganuma, T., Swanson, S.K., Lee, K.K., Shia, W.J., Anderson, S., Yates, J., Washburn, M.P., et al. (2005). Histone H3 methylation by Set2 directs deacetylation of coding regions by Rpd3S to suppress spurious intragenic transcription. Cell *123*, 581–592.

Comerford, S.A., Huang, Z., Du, X., Wang, Y., Cai, L., Witkiewicz, A.K., Walters, H., Tantawy, M.N., Fu, A., Manning, H.C., et al. (2014). Acetate dependence of tumors. Cell *159*, 1591–1602.

DeLong, C.J., Shen, Y.J., Thomas, M.J., and Cui, Z. (1999). Molecular distinction of phosphatidylcholine synthesis between the CDP-choline pathway and phosphatidylethanolamine methylation pathway. J. Biol. Chem. *274*, 29683–29688.

Fnu, S., Williamson, E.A., De Haro, L.P., Brenneman, M., Wray, J., Shaheen, M., Radhakrishnan, K., Lee, S.H., Nickoloff, J.A., and Hromas, R. (2011). Methylation of histone H3 lysine 36 enhances DNA repair by nonhomologous end-joining. Proc. Natl. Acad. Sci. U S A *108*, 540–545.

Haider, A., Wei, Y.C., Lim, K., Barbosa, A.D., Liu, C.H., Weber, U., Mlodzik, M., Oras, K., Collier, S., Hussain, M.M., et al. (2018). PCYT1A regulates phosphatidylcholine homeostasis from the inner nuclear membrane in response to membrane stored curvature elastic stress. Dev. Cell *45*, 481–495.e8.

Henry, S.A., Kohlwein, S.D., and Carman, G.M. (2012). Metabolism and regulation of glycerolipids in the yeast Saccharomyces cerevisiae. Genetics *190*, 317–349.

Hsieh, W.C., Sutter, B.M., Ruess, H., Barnes, S.D., Malladi, V.S., and Tu, B.P. (2022). Glucose starvation induces a switch in the histone acetylome for activation of gluconeogenic and fat metabolism genes. Mol. Cell *82*, 60–74.e5.

Kaiser, H.J., Surma, M.A., Mayer, F., Levental, I., Grzybek, M., Klemm, R.W., Da Cruz, S., Meisinger, C., Muller, V., Simons, K., et al. (2011). Molecular convergence of bacterial and eukaryotic surface order. J. Biol. Chem. *286*, 40631–40637.

Kim, W., Deik, A., Gonzalez, C., Gonzalez, M.E., Fu, F., Ferrari, M., Churchhouse, C.L., Florez, J.C., Jacobs, S.B.R., Clish, C.B., et al. (2019). Polyunsaturated fatty acid desaturation is a mechanism for glycolytic NAD(+) recycling. Cell Metabol. *29*, 856–870.e7.

Koundouros, N., and Poulogiannis, G. (2020). Reprogramming of fatty acid metabolism in cancer. Br. J. Cancer *122*, 4–22.

Laxman, S., Sutter, B.M., Wu, X., Kumar, S., Guo, X., Trudgian, D.C., Mirzaei, H., and Tu, B.P. (2013). Sulfur amino acids regulate translational capacity and

metabolic homeostasis through modulation of tRNA thiolation. Cell *154*, 416–429.

Lee, C.H., Wu, J., and Li, B. (2013). Chromatin remodelers fine-tune H3K36me-directed deacetylation of neighbor nucleosomes by Rpd3S. Mol. Cell *52*, 255–263.

Liu, S., Fu, S., Wang, G., Cao, Y., Li, L., Li, X., Yang, J., Li, N., Shan, Y., Cao, Y., et al. (2021). Glycerol-3-phosphate biosynthesis regenerates cytosolic NAD(+) to alleviate mitochondrial disease. Cell Metab. *33*, 1974–1987.e9.

Loewen, C.J., Gaspar, M.L., Jesch, S.A., Delon, C., Ktistakis, N.T., Henry, S.A., and Levine, T.P. (2004). Phospholipid metabolism regulated by a transcription factor sensing phosphatidic acid. Science *304*, 1644–1647.

Longtine, M.S., McKenzie, A., 3rd, Demarini, D.J., Shah, N.G., Wach, A., Brachat, A., Philippsen, P., and Pringle, J.R. (1998). Additional modules for versatile and economical PCR-based gene deletion and modification in Saccharomyces cerevisiae. Yeast *14*, 953–961.

Lou, W., Ting, H.C., Reynolds, C.A., Tyurina, Y.Y., Tyurin, V.A., Li, Y., Ji, J., Yu, W., Liang, Z., Stoyanovsky, D.A., et al. (2018). Genetic re-engineering of polyunsaturated phospholipid profile of Saccharomyces cerevisiae identifies a novel role for Cld1 in mitigating the effects of cardiolipin peroxidation. Biochim. Biophys. Acta Mol. Cell Biol. Lipids *1863*, 1354–1368.

McDaniel, S.L., Hepperla, A.J., Huang, J., Dronamraju, R., Adams, A.T., Kulkarni, V.G., Davis, I.J., and Strahl, B.D. (2017). H3K36 methylation regulates nutrient stress response in saccharomyces cerevisiae by enforcing transcriptional fidelity. Cell Rep. *19*, 2371–2382.

Pang, Z., Chong, J., Zhou, G., de Lima Morais, D.A., Chang, L., Barrette, M., Gauthier, C., Jacques, P.E., Li, S., and Xia, J. (2021). MetaboAnalyst 5.0: narrowing the gap between raw spectra and functional insights. Nucleic Acids Res. *49*, W388–W396.

Pryde, F., Jain, D., Kerr, A., Curley, R., Mariotti, F.R., and Vogelauer, M. (2009). H3 k36 methylation helps determine the timing of cdc45 association with replication origins. PLoS One *4*, e5882.

Pu, M., Ni, Z., Wang, M., Wang, X., Wood, J.G., Helfand, S.L., Yu, H., and Lee, S.S. (2015). Trimethylation of Lys36 on H3 restricts gene expression change during aging and impacts life span. Genes Dev. *29*, 718–731.

Renne, M.F., Bao, X., Hokken, M.W., Bierhuizen, A.S., Hermansson, M., Sprenger, R.R., Ewing, T.A., Ma, X., Cox, R.C., Brouwers, J.F., et al. (2021). Molecular species selectivity of lipid transport creates a mitochondrial sink for di-unsaturated phospholipids. EMBO J., e106837.

Romanauska, A., and Kohler, A. (2018). The inner nuclear membrane is a metabolically active territory that generates nuclear lipid droplets. Cell *174*, 700–715.

Romanauska, A., and Köhler, A. (2021). Reprogrammed lipid metabolism protects inner nuclear membrane against unsaturated fat. Dev. Cell *56*, 2562–2578.e3.

Ruiz, M., Bodhicharla, R., Svensk, E., Devkota, R., Busayavalasa, K., Palmgren, H., Stahlman, M., Boren, J., and Pilon, M. (2018). Membrane fluidity is regulated by the C-elegans transmembrane protein FLD-1 and its human homologs TLCD1/2. Elife *7*, e40686.

Schuck, S., Honsho, M., Ekroos, K., Shevchenko, A., and Simons, K. (2003). Resistance of cell membranes to different detergents. Proc. Natl. Acad. Sci. U S A *100*, 5795–5800.

Sen, P., Dang, W., Donahue, G., Dai, J., Dorsey, J., Cao, X., Liu, W., Cao, K., Perry, R., Lee, J.Y., et al. (2015). H3K36 methylation promotes longevity by enhancing transcriptional fidelity. Genes Dev. *29*, 1362–1376.

Sinensky, M. (1974). Homeoviscous adaptation–a homeostatic process that regulates the viscosity of membrane lipids in Escherichia coli. Proc. Natl. Acad. Sci. U S A *71*, 522–525.

Singh, P. (2016). Budding yeast: an ideal backdrop for in vivo lipid biochemistry. Front Cell Dev Biol *4*, 156.

Singh, P., Ramachandran, S.K., Zhu, J., Kim, B.C., Biswas, D., Ha, T., Iglesias, P.A., and Li, R. (2017). Sphingolipids facilitate age asymmetry of membrane proteins in dividing yeast cells. Mol. Biol. Cell *28*, 2712–2722.

Sivanand, S., Viney, I., and Wellen, K.E. (2018). Spatiotemporal control of acetyl-CoA metabolism in chromatin regulation. Trends Biochem. Sci. *43*, 61–74.

Sorenson, M.R., Jha, D.K., Ucles, S.A., Flood, D.M., Strahl, B.D., Stevens, S.W., and Kress, T.L. (2016). Histone H3K36 methylation regulates pre-mRNA splicing in Saccharomyces cerevisiae. RNA Biol. *13*, 412–426.

Sutter, B.M., Wu, X., Laxman, S., and Tu, B.P. (2013). Methionine inhibits autophagy and promotes growth by inducing the SAM-responsive methylation of PP2A. Cell *154*, 403–415.

Toulmay, A., and Prinz, W.A. (2013). Direct imaging reveals stable, micrometer-scale lipid domains that segregate proteins in live cells. J. Cell Biol. *202*, 35–44.

Tu, B.P., Mohler, R.E., Liu, J.C., Dombek, K.M., Young, E.T., Synovec, R.E., and McKnight, S.L. (2007). Cyclic changes in metabolic state during the life of a yeast cell. Proc. Natl. Acad. Sci. U S A *104*, 16886–16891.

van Dijken, J.P., Bauer, J., Brambilla, L., Duboc, P., Francois, J.M., Gancedo, C., Giuseppin, M.L., Heijnen, J.J., Hoare, M., Lange, H.C., et al. (2000). An interlaboratory comparison of physiological and genetic properties of four Saccharomyces cerevisiae strains. Enzyme Microb. Technol. *26*, 706–714.

van Meer, G., Voelker, D.R., and Feigenson, G.W. (2008). Membrane lipids: where they are and how they behave. Nat. Rev. Mol. Cell Biol. *9*, 112–124.

Wen, H., Li, Y.Y., Xi, Y.X., Jiang, S.M., Stratton, S., Peng, D.N., Tanaka, K., Ren, Y.F., Xia, Z., Wu, J., et al. (2014). ZMYND11 links histone H3.3K36me3 to transcription elongation and tumour suppression. Nature *508*, 263–268.

Xu, Z., Wei, W., Gagneur, J., Perocchi, F., Clauder-Munster, S., Camblong, J., Guffanti, E., Stutz, F., Huber, W., and Steinmetz, L.M. (2009). Bidirectional promoters generate pervasive transcription in yeast. Nature *457*, 1033–1037.

Ye, C., Bandara, W.M., and Greenberg, M.L. (2013). Regulation of inositol metabolism is fine-tuned by inositol pyrophosphates in Saccharomyces cerevisiae. J. Biol. Chem. *288*, 24898–24908.

Ye, C., Sutter, B.M., Wang, Y., Kuang, Z., and Tu, B.P. (2017). A metabolic function for phospholipid and histone methylation. Mol. Cell *66*, 180–193.e8.

Ye, C., Sutter, B.M., Wang, Y., Kuang, Z., Zhao, X., Yu, Y., and Tu, B.P. (2019). Demethylation of the protein phosphatase PP2A promotes demethylation of histones to enable their function as a methyl group sink. Mol. Cell *73*, 1115–1126.e6.

Ye, C., and Tu, B.P. (2018). Sink into the epigenome: histones as repositories that influence cellular metabolism. Trends Endocrinol. Metabol. *29*, 626–637.

Young, B.P., Shin, J.J.H., Orij, R., Chao, J.T., Li, S.C., Guan, X.L., Khong, A., Jan, E., Wenk, M.R., Prinz, W.A., et al. (2010). Phosphatidic acid is a pH biosensor that links membrane biogenesis to metabolism. Science *329*, 1085–1088.

Yuan, M., Breitkopf, S.B., Yang, X., and Asara, J.M. (2012). A positive/negative ion-switching, targeted mass spectrometry-based metabolomics platform for bodily fluids, cells, and fresh and fixed tissue. Nat. Protoc. *7*, 872–881.

Zhang, Y.M., and Rock, C.O. (2008). Membrane lipid homeostasis in bacteria. Nat. Rev. Microbiol. *6*, 222–233.

STAR★METHODS

KEY RESOURCES TABLE

REAGENT or RESOURCE	SOURCE	IDENTIFIER
Antibodies		
Mouse anti-FLAG M2 antibody	Sigma	Cat#F3165; RRID: AB_259529
Rat Anti-Sah1	This manuscript	N/A
Rabbit anti-H3K4me3	Millipore	Cat# 07-473, RRID: AB_1977252
Rabbit anti-H3K36me1	Abcam	Cat# ab9048, RRID: AB_306964
Rabbit anti-H3K36me2	Abcam	Cat# ab9049, RRID: AB_1280939
Rabbit anti-H3K36me3	Abcam	Cat# ab9050, RRID: AB_306966
Rabbit anti-H3K79me3	Abcam	Cat# ab2621, RRID: AB_303215
Mouse anti-GFP	Roche	Cat# 11814460
Rabbit anti-H3	Millipore	Cat#06-755
Rabbit anti-G6PDH	Sigma	Cat#A9521
Mouse anti-HA(12CA5)	Roche	Ref#11583816001
Rabbit anti-HA (C29F4)	Cell Signaling Technology	Cat# 3724S RRID: AB_10693385
Chemicals, peptides, and recombinant proteins		
Triton X-100	Sigma	Cat#9002-93-1
Methionine	Sigma	Cat#M9625
Uridine	Sigma	Cat#58-96-8
Cytidine	sigma	Cat#65-46-3
Uracil	Sigma	Cat#66-22-8
(15NH4)2SO4	Cambridge Isotope	NLM-713-PK
phenylmethylsulfonyl fluroride	Sigma	Cat#P7626
sodium orthovanadate	MP Biomedicals	Cat#159664
Pierce BCA protein assay	Thermo Fisher Scientific	Cat#23225
cOmplete EDTA-free protease inhibitor cocktail tablets	Roche	Cat#11873580001
14:0 PS (1,2-Dimyristoyl-sn-glycero-3-phospho-L-serine sodium salt)	Avanti Polar Lipids	Cat#105405
17:0 PC (1,2-diheptadecanoyl-sn-glycero-3-phosphocholine)	Avanti Polar Lipids	Cat#70897
17:0 PE (1,2-diheptadecanoyl-sn-glycero-3-phosphoethanolamine)	Avanti Polar Lipids	Cat#140219
Deposited data		
RNA-seq data WT, rph1Δ, set2Δ, H3K36A	GEO-NCBI	GSE181620
RNA-seq data WT, set2Δ, cho2Δ, opi1Δ, set2Δcho2Δ, set2Δopi1Δ	GEO-NCBI	GSE193198
targeted metabolomics data	Mendeley Data	https://doi.org/10.17632/t3tng8fbnn.1
Experimental models: Organisms/strains		
S. cerevisiae: Name = CEN.PK; Genotype = MATa	van Dijken et al., 2000	N/A
S. cerevisiae: Name = CEN.PK; Genotype = MATα	van Dijken et al., 2000	N/A
S. cerevisiae: Name = CEN.PK; Genotype = MATa; cho2Δ::KanMX	Ye et al. (2017)	N/A
S. cerevisiae: Name = CEN.PK; Genotype = MATa; opi1Δ::KanMX	Ye et al. (2017)	N/A
S. cerevisiae: Name = CEN.PK; Genotype = MATa; set2Δ::HYG	Ye et al. (2017)	N/A

(*Continued on next page*)

Continued

REAGENT or RESOURCE	SOURCE	IDENTIFIER
S. cerevisiae: Name = CEN.PK; Genotype = MATa; set1Δ::HYG	Ye et al. (2017)	N/A
S. cerevisiae: Name = CEN.PK; Genotype = MATalpha; dot1Δ::HYG	Ye et al. (2017)	N/A
S. cerevisiae: Name = CEN.PK; Genotype = MATa; set1Δ::HYG; set2Δ::KanMX	Ye et al. (2017)	N/A
S. cerevisiae: Name = CEN.PK; Genotype = MATa; set2Δ::HYG; dot1Δ::KanMX	Ye et al. (2017)	N/A
S. cerevisiae: Name = CEN.PK; Genotype = MATa; set1Δ::HYG; dot1Δ::HYG; set2Δ::KanMX	This manuscript	N/A
S. cerevisiae: Name = CEN.PK; Genotype = MATα; H3K36A HHT1_K36A::HYG HHT2_K36A::NAT	Ye et al. (2017)	N/A
S. cerevisiae: Name = CEN.PK; Genotype = MATa; cho2Δ::KanMX; set2Δ::HYG	This manuscript	N/A
S. cerevisiae: Name = CEN.PK; Genotype = MATa; opi1Δ::KanMX; set2Δ::HYG	This manuscript	N/A
S. cerevisiae: Name = CEN.PK; Genotype = MATa; ura1Δ::KanMX	This manuscript	N/A
S. cerevisiae: Name = CEN.PK; Genotype = MATa; ura2Δ::KanMX	This manuscript	N/A
S. cerevisiae: Name = CEN.PK; Genotype = MATa; ura3Δ::KanMX	This manuscript	N/A
S. cerevisiae: Name = CEN.PK; Genotype = MATa; ura1Δ::KanMX; set2Δ::HYG	This manuscript	N/A
S. cerevisiae: Name = CEN.PK; Genotype = MATa; ura2Δ::KanMX; set2Δ::HYG	This manuscript	N/A
S. cerevisiae: Name = CEN.PK; Genotype = MATa; ura3Δ::KanMX; set2Δ::HYG	This manuscript	N/A
S. cerevisiae: Name = CEN.PK; Genotype = MATa; pct1Δ::NAT; set2Δ::HYG	This manuscript	N/A
S. cerevisiae: Name = CEN.PK; Genotype = MATa; pct1Δ::NAT; cho2Δ::KanMX; set2Δ::HYG	This manuscript	N/A
S. cerevisiae: Name = CEN.PK; Genotype = MATa; met6Δ::NAT; cho2Δ::KanMX; set2Δ::HYG	This manuscript	N/A
S. cerevisiae: Name = CEN.PK; Genotype = MATa; met6Δ::NAT; opi1Δ::KanMX; set2Δ::HYG	This manuscript	N/A
S. cerevisiae: Name = CEN.PK; Genotype = MATa; met6Δ::KanMX	This manuscript	N/A
S. cerevisiae: Name = CEN.PK; Genotype = MATα; met6Δ::KanMX; set2Δ::HYG	This manuscript	N/A
S. cerevisiae: Name = CEN.PK; Genotype = MATa; MET1-FLAG::NAT	This manuscript	N/A
S. cerevisiae: Name = CEN.PK; Genotype = MATa; MET3-FLAG::NAT	This manuscript	N/A
S. cerevisiae: Name = CEN.PK; Genotype = MATα; MET5-FLAG::NAT	This manuscript	N/A
S. cerevisiae: Name = CEN.PK; Genotype = MATa; MET6-FLAG::NAT	This manuscript	N/A
S. cerevisiae: Name = CEN.PK; Genotype = MATa; MET7-FLAG::NAT	This manuscript	N/A
S. cerevisiae: Name = CEN.PK; Genotype = MATa; MET10-FLAG::NAT	This manuscript	N/A
S. cerevisiae: Name = CEN.PK; Genotype = MATa; MET14-FLAG::NAT	This manuscript	N/A
S. cerevisiae: Name = CEN.PK; Genotype = MATa; MET16-FLAG::NAT	This manuscript	N/A
S. cerevisiae: Name = CEN.PK; Genotype = MATa; MET17-FLAG::NAT	This manuscript	N/A
S. cerevisiae: Name = CEN.PK; Genotype = MATa; SAM1-FLAG::NAT	This manuscript	N/A
S. cerevisiae: Name = CEN.PK; Genotype = MATa; SAM2-FLAG::NAT	This manuscript	N/A
S. cerevisiae: Name = CEN.PK; Genotype = MATa; Cys3-FLAG::NAT	This manuscript	N/A
S. cerevisiae: Name = CEN.PK; Genotype = MATa; Cys4-FLAG::NAT	This manuscript	N/A
S. cerevisiae: Name = CEN.PK; Genotype = MATa; STR2-FLAG::NAT	This manuscript	N/A
S. cerevisiae: Name = CEN.PK; Genotype = MATa; STR3-FLAG::NAT	This manuscript	N/A

(*Continued on next page*)

Continued

REAGENT or RESOURCE	SOURCE	IDENTIFIER
S. cerevisiae: Name = CEN.PK; Genotype = MATa; cho2Δ::KanMX; MET1-FLAG::NAT	This manuscript	N/A
S. cerevisiae: Name = CEN.PK; Genotype = MATa; cho2Δ::KanMX; MET3-FLAG::NAT	This manuscript	N/A
S. cerevisiae: Name = CEN.PK; Genotype = MATa; cho2Δ::KanMX; MET5-FLAG::NAT	This manuscript	N/A
S. cerevisiae: Name = CEN.PK; Genotype = MATa; cho2Δ::KanMX; MET6-FLAG::NAT	This manuscript	N/A
S. cerevisiae: Name = CEN.PK; Genotype = MATa; cho2Δ::KanMX; MET7-FLAG::NAT	This manuscript	N/A
S. cerevisiae: Name = CEN.PK; Genotype = MATa; cho2Δ::KanMX; MET10-FLAG::NAT	This manuscript	N/A
S. cerevisiae: Name = CEN.PK; Genotype = MATa; cho2Δ::KanMX; MET14-FLAG::NAT	This manuscript	N/A
S. cerevisiae: Name = CEN.PK; Genotype = MATa; cho2Δ::KanMX; MET16-FLAG::NAT	This manuscript	N/A
S. cerevisiae: Name = CEN.PK; Genotype = MATa; cho2Δ::KanMX; MET17-FLAG::NAT	This manuscript	N/A
S. cerevisiae: Name = CEN.PK; Genotype = MATa; cho2Δ::KanMX; SAM1-FLAG::NAT	This manuscript	N/A
S. cerevisiae: Name = CEN.PK; Genotype = MATa; cho2Δ::KanMX; SAM2-FLAG::NAT	This manuscript	N/A
S. cerevisiae: Name = CEN.PK; Genotype = MATa; cho2Δ::KanMX; CYS3-FLAG::NAT	This manuscript	N/A
S. cerevisiae: Name = CEN.PK; Genotype = MATa; cho2Δ::KanMX; CYS4-FLAG::NAT	This manuscript	N/A
S. cerevisiae: Name = CEN.PK; Genotype = MATa; cho2Δ::KanMX; STR2-FLAG::NAT	This manuscript	N/A
S. cerevisiae: Name = CEN.PK; Genotype = MATa; cho2Δ::KanMX; STR3-FLAG::NAT	This manuscript	N/A
S. cerevisiae: Name = CEN.PK; Genotype = MATa; opi1Δ::KanMX; MET1-FLAG::NAT	This manuscript	N/A
S. cerevisiae: Name = CEN.PK; Genotype = MATa; opi1Δ::KanMX; MET3-FLAG::NAT	This manuscript	N/A
S. cerevisiae: Name = CEN.PK; Genotype = MATa; opi1Δ::KanMX; MET5-FLAG::NAT	This manuscript	N/A
S. cerevisiae: Name = CEN.PK; Genotype = MATa; opi1Δ::KanMX; MET6-FLAG::NAT	This manuscript	N/A
S. cerevisiae: Name = CEN.PK; Genotype = MATa; opi1Δ::KanMX; MET7-FLAG::NAT	This manuscript	N/A
S. cerevisiae: Name = CEN.PK; Genotype = MATa; opi1Δ::KanMX; MET10-FLAG::NAT	This manuscript	N/A
S. cerevisiae: Name = CEN.PK; Genotype = MATa; opi1Δ::KanMX; MET14-FLAG::NAT	This manuscript	N/A
S. cerevisiae: Name = CEN.PK; Genotype = MATa; opi1Δ::KanMX; MET16-FLAG::NAT	This manuscript	N/A
S. cerevisiae: Name = CEN.PK; Genotype = MATa; opi1Δ::KanMX; MET17-FLAG::NAT	This manuscript	N/A
S. cerevisiae: Name = CEN.PK; Genotype = MATa; opi1Δ::KanMX; SAM1-FLAG::NAT	This manuscript	N/A
S. cerevisiae: Name = CEN.PK; Genotype = MATa; opi1Δ::KanMX; SAM2-FLAG::NAT	This manuscript	N/A
S. cerevisiae: Name = CEN.PK; Genotype = MATa; opi1Δ::KanMX; CYS3-FLAG::NAT	This manuscript	N/A
S. cerevisiae: Name = CEN.PK; Genotype = MATa; opi1Δ::KanMX; CYS4-FLAG::NAT	This manuscript	N/A
S. cerevisiae: Name = CEN.PK; Genotype = MATa; opi1Δ::KanMX; STR2-FLAG::NAT	This manuscript	N/A
S. cerevisiae: Name = CEN.PK; Genotype = MATa; opi1Δ::KanMX; STR3-FLAG::NAT	This manuscript	N/A
S. cerevisiae: Name = CEN.PK; Genotype = MATa; set2Δ::HYG; MET1-FLAG::NAT	This manuscript	N/A
S. cerevisiae: Name = CEN.PK; Genotype = MATa; set2Δ::HYG; MET3-FLAG::NAT	This manuscript	N/A
S. cerevisiae: Name = CEN.PK; Genotype = MATa; set2Δ::HYG; MET5-FLAG::NAT	This manuscript	N/A
S. cerevisiae: Name = CEN.PK; Genotype = MATa; set2Δ::HYG; MET6-FLAG::NAT	This manuscript	N/A
S. cerevisiae: Name = CEN.PK; Genotype = MATa; set2Δ::HYG; MET7-FLAG::NAT	This manuscript	N/A
S. cerevisiae: Name = CEN.PK; Genotype = MATa; set2Δ::HYG; MET10-FLAG::NAT	This manuscript	N/A
S. cerevisiae: Name = CEN.PK; Genotype = MATa; set2Δ::HYG; MET14-FLAG::NAT	This manuscript	N/A
S. cerevisiae: Name = CEN.PK; Genotype = MATa; set2Δ::HYG; MET16-FLAG::NAT	This manuscript	N/A
S. cerevisiae: Name = CEN.PK; Genotype = MATa; set2Δ::HYG; MET17-FLAG::NAT	This manuscript	N/A
S. cerevisiae: Name = CEN.PK; Genotype = MATa; set2Δ::HYG; SAM1-FLAG::NAT	This manuscript	N/A
S. cerevisiae: Name = CEN.PK; Genotype = MATa; set2Δ::HYG; SAM2-FLAG::NAT	This manuscript	N/A
S. cerevisiae: Name = CEN.PK; Genotype = MATa; set2Δ::HYG; CYS3-FLAG::NAT	This manuscript	N/A
S. cerevisiae: Name = CEN.PK; Genotype = MATa; set2Δ::HYG; CYS4-FLAG::NAT	This manuscript	N/A
S. cerevisiae: Name = CEN.PK; Genotype = MATa; set2Δ::HYG; STR2-FLAG::NAT	This manuscript	N/A
S. cerevisiae: Name = CEN.PK; Genotype = MATa; set2Δ::HYG; STR3-FLAG::NAT	This manuscript	N/A
S. cerevisiae: Name = CEN.PK; Genotype = MATα; MRH1-GFP::HYG	This manuscript	N/A
S. cerevisiae: Name = CEN.PK; Genotype = MATα; set2Δ::NAT; MRH1-GFP::HYG	This manuscript	N/A
S. cerevisiae: Name = CEN.PK; Genotype = MATα; cho2Δ::KanMX; H3K36A HHT1_K36A::HYG HHT2_K36A::NAT	This manuscript	N/A

(*Continued on next page*)

Continued

REAGENT or RESOURCE	SOURCE	IDENTIFIER
S. cerevisiae: Name = CEN.PK; Genotype = MATα; opi1Δ::KanMX; H3K36A HHT1_K36A::HYG HHT2_K36A::NAT	This manuscript	N/A
S. cerevisiae: Name = CEN.PK; Genotype = MATα; rph1Δ::NAT	Ye et al. (2019)	N/A
Software and algorithms		
MetaboAnalyst 5.0	Pang et al. (2021)	N/A

RESOURCE AVAILABILITY

Lead contact

Further information and requests for reagents may be directed to and will be fulfilled by the corresponding author, Dr. Cunqi Ye (yecunqi@zju.edu.cn).

Materials availability

All the yeast strains generated in this study are available upon request.

Data and code availability

- The RNA-seq datasets generated in this study are available at NCBI GEO:GSE181620 and GEO:GSE193198. The dataset of targeted metabolomics analysis is available at Mendeley Data (https://doi.org/10.17632/t3tng8fbnn.1).
- This paper does not report original code.
- Any additional information required to reanalyze the data reported in this paper is available from the lead contact upon request.

EXPERIMENTAL MODEL AND SUBJECT DETAILS

All yeast strains used in this study are listed in the Key resources table. All strains and genetic manipulations were verified by sequencing and phenotype. The prototrophic CEN.PK strain background was used in all experiments. Gene deletions were carried out using either tetrad dissection or standard PCR-based strategies to amplify resistance cassettes with appropriate flanking sequences, and replacing the target gene by homologous recombination (Longtine et al., 1998). Carboxy-terminal tags were similarly made with the PCR-based method to amplify resistance cassettes with flanking sequences.

Media used in this study: Rich medium YPL (2% yeast extract, 2% peptone and 2% lactate) and minimal medium SL (0.17% yeast nitrogen base without amino acids containing 0.5% ammonium sulfate (Difco), 2% lactate).

METHOD DETAILS

Determination of survival rates

Starvation was done by switching yeast cells growing exponentially in YPL to SL. To measure survival rates, an aliquot of liquid culture was taken, diluted, and spread on YP glucose plates for colony formation after 12 h, 24 h, and other indicated times. The rate of survival was calculated by the following formula: Survival rate% = 100* the number of colonies at an indicated time * dilution factor/(number of colonies at 12 h * dilution factor). Of note, after the switch, cells proliferated very slowly under starvation. At 12 h, the optical density (OD) at 600 nm and the number of colonies formed per OD were similar among WT and the mutant strains, which ensures an appropriate normalization point for survival rate calculation. To examine the effects of fatty acids on survival under starvation, cells were cultured in YPL containing 1 mM oleic acid or 1 mM stearic acid. The logarithmically growing cells were collected by centrifugation, washed, and resuspended in SL containing 1 mM of the same fatty acid supplemented in YPL. After 12 h and 24 h, an aliquot of cell culture was used to assess viable cells for calculating survival rates.

Determination of growth rates of yeast cells by absorbance at 600 nm or spotting assay

For the determination of cell growth in Figure 4D, yeast cells cultured overnight in a nutrient-limiting medium containing 5% YPL and 95% SL were diluted to 0.1 of OD_{600} in fresh YPL or a modified medium mixed with 1% YPL and 99% SL. 1 mM uracil, uridine (U), and cytidine (C) were supplemented to this modified medium in another experiment shown in Figure 4E. Cell growth was monitored by absorbance reading at 600 nm using a spectrometer from MAPADA (Model P6).

For spotting assay in Figure 2J, cells pre-cultured in YPL overnight to stationary phase were diluted to 0.1 of A_{600} in fresh YPL with or without 3 mM oleic acid or stearic acid supplementation. When cells grew to the logarithmic phase (OD_{600} = ~1.0), 3 μL aliquots of a series of 10-fold dilutions from 0.5 OD_{600} were spotted onto YPL plates with or without 1% Triton X-100 and incubated for about

2 days at indicated temperatures (30°C or 37°C). For Figure 4F, cells were pre-cultured in YPL overnight to stationary phase, and 3 μL aliquots of a series of 10-fold dilutions from 0.5 OD_{600} were spotted onto YPL plates and incubated for about 2 days at 30°C.

Lipid extraction and quantification

Yeast lipids were extracted with chloroform/methanol (2:1) (v/v) as described previously (Ye et al., 2013). In brief, 10 OD_{600} units of yeast cells were harvested for lipid extraction. Cell pellets were resuspended in 0.5 mL mass spectrometry (MS)-grade methanol and lysed by bead-beading. Cell pellets and lysates were then transferred to glass tubes. Chloroform and citric acid were used to achieve phase separation, and the bottom lipid phase was collected and dried using a vacuum concentrator system (Labconco).

Lipid extracts were dissolved in a mixed MS grade solution containing isopropanol, acetonitrile, water (2:1:1), and 17:0 PC, 17:0 PE, and 14:0 PS used as spike-in standards. 5 uL of 50-fold dilutions of these lipid samples were injected for quantitative analysis by LC-MS/MS with a triple quadrupole mass spectrometer (the QTRAP 6500 + System, AB SCIEX). Phospholipids separated chromatographically on a C18 column (ACQUITY UPLC BEH C18 column, 130A, 1.7 μm, 2.1 mm × 50 mm) were followed by quantification using multiple reaction monitoring (MRM) transitions of mass spectrometry. Specifically, liquid chromatography was programmed below: Buffer A contains 33.3% methanol, 33.3% acetonitrile, 33.4% water, 5 mM ammonium acetate, and Buffer B contains 5 mM ammonium acetate in 100% isopropanol. Flow rate was 0.15 mL/min using the following method: T = 0 min, 20% B; T = 1 min, 20% B; T = 3 min, 60% B; T = 13 min, 98% B; T = 13.1 min, 20% B, T = 16 min, 20% B. The retention time for each MRM peak was compared to an appropriate standard. The area under each peak was then quantitated using Analyst software, reinspected for accuracy.

Determination of plasma membrane fluidity by fluorescence recovery after photo bleaching (FRAP) measurement

The membrane protein Mrh1 was appended with a GFP tag to the C-terminus of its chromosomal locus. WT and *set2Δ* strains containing GFP-tagged Mrh1 were cultured in rich medium to log phase and imaged with a ZEISS LSM880 laser scanning confocal microscope. The Plan-Apochromat 63x/1.4 oil objective lens (Zeiss) was used. Images were recorded by scanning the laser over a 67.5μm * 67.5 μm area with an image size of 512 * 512 pixels and scan speed set to 8. GFP fluorescence signals were collected over time. The fluorescence intensity of a bleached area was obtained by ZEN software black edition (ZEISS). FRAP that measures lateral diffusion of this fluorescent membrane protein reflects plasma membrane fluidity (Singh et al., 2017). To compare plasma membrane fluidity in WT and *set2Δ* cells, we normalized fluorescence intensity recovered after photobleach to before.

Determination of membrane order with Laurdan

Yeast cells logarithmically growing in YPL or 12 h after the switch to SL were collected and spheroplasted with 1 mg/mL zymolyase in 1 M sorbitol. The spheroplasts were incubated with 1 μM Laurdan at 30°C for 30 min. Samples were excited at 360 nm using a SynergyNEO2 Multiscan Spectrum (Biotek), and fluorescence intensities were measured at 440 nm and 490 nm. The Laurdan GP value was calculated: $GP = (I_{440}\text{-}I_{490})/(I_{440}\text{-}I_{490})$. The background of the laurdan-containing buffer was subtracted from emission values (Kaiser et al., 2011).

RNA-seq analysis

RNA isolation of yeast cells under different growth conditions was carried out following the manufacturer's manual using the MasterPure yeast RNA purification kit (Epicenter). RNA concentration was determined by absorbance at 260 nm. 1 μg RNA was reverse transcribed to cDNA using HiScript III first Strand cDNA Synthesis Kit (Vazyme). RNA samples were prepared in two biological replicates as described above. Library construction and sequencing were performed by Genewiz. Detailed procedures can be found from the following website: https://cdn2.hubspot.net/hubfs/3478602/NGS/RNA-Seq/GENEWIZ_RNA-Seq_Technical_Specifications_US.pdf.

Metabolite extraction and quantitation

Intracellular metabolites were extracted using a previously established method (Tu et al., 2007). Care was taken to quench cells quickly and maintain metabolites in acid to minimize oxidation. Briefly, equal OD units of cells were rapidly quenched to stop metabolism by adding 4 volumes of quenching buffer containing 60% methanol and 10 mM Tricine, pH 7.4 that was pre-cooled to −40°C. 5 min after holding at −40°C, cells were spun at 5,000 g for 3 min at 0°C, washed with the same buffer, and then resuspended in 1 mL extraction buffer containing 75% ethanol and 0.5 mM Tricine, pH 7.4. Intracellular metabolites were extracted by incubating at 75°C for 3 min, then chilling on ice for 5 min. Samples were spun at 20,000 g for 1 min to pellet cell debris, and 0.9 mL of the supernatant was transferred to a new tube. After a second spin at 20,000 g for 10 min, 0.8 mL of the supernatant was transferred to a new tube. Metabolites in the extraction buffer were dried using a vacuum concentrator system (Labconco) and stored at −80°C until analysis. Dried metabolite extracts were resuspended in either 60% acetonitrile or 10 mM tributylamine for injection according to specific LC methods used below.

Cellular metabolites were quantitated by LC-MS/MS with a triple quadrupole mass spectrometer (the QTRAP 6500 + System, ABSCIEX) using previously established methods (Ye et al., 2017; Yuan et al., 2012). Briefly, metabolites were separated chromatographically on a SeQuant Zic-pHILIC column (5 μm polymer 150 × 2.1 mm, Millipore Sigma) or a C18-based column

with polar embedded groups (Synergi Fusion-RP, 15,032.00mm4 micron, Phenomenex), using a high-performance UHPLC system (Exion LC AD system) coupled to a triple quadrupole mass spectrometer (QTRAP 6500 + System, AB SCIEX).

For targeted metabolomics, we performed a 34-min liquid chromatography on the pHILIC column at a flow rate of 0.15 mL/min, with 20 mM ammonium carbonate and 0.1% (v/v) ammonium hydroxide as Solvent A and acetonitrile as Solvent B. The following gradient was employed: 0.01 min 80% B, 20 min 20% B, 20.5 min 80% B, 34 min 80% B. Metabolites were detected by MRM transitions in positive and negative modes. For better separation of some metabolites, such as nucleotides, we employed another LC method on the C18 column. Specifically, we performed a 22-min run at a flow rate of 0.5 mL/min.10 mM tributylamine (pH 5.0) in water was used as Solvent A and methanol as Solvent B. The following gradient elution was performed: 0.01 min, 0% B, 4 min, 0% B, 11 min, 50% B, 13 min, 100% B, 17 min, 100% B, 18 min, 0% B, 22 min, 0% B. It should be noted that yeast metabolites from different strains in a single experiment were always compared and analyzed simultaneously and therefore the relative abundance is directly comparable.

Metabolic flux analysis using ^{15}N ammonium sulfate

^{15}N labeled ammonium sulfate ($(^{15}NH_4)_2SO_4$) was obtained from Cambridge Isotope Laboratories, Inc. Cells logarithmically grown in YPL were spun down, washed with synthetic minimal media without ammonium sulfate, and re-suspended to SL medium where all the ammonium sulfate (sole nitrogen source) was ^{15}N labeled. Cells were collected at indicated times, and metabolites were extracted. ^{15}N labeled metabolites were detected by LC-MS/MS, with the targeted parent and daughter ions specific to the ^{15}N form of the metabolites.

Whole yeast cell extracts preparation and western blotting

A urea-based protocol was used to lyse yeast cells for western blots. Cells were spun down, quenched in 20% trichloroacetic acid on ice for 15 min, washed with acetone. Cell pellets were resuspended in urea buffer containing 50 mM Tris-Cl pH 7.5, 5 mM EDTA, 6 M urea, 1% SDS, 1mM PMSF, 2 mM sodium orthovanadate, and 50 mM NaF, and lysed by bead-beating. After collecting supernatants, protein concentration was determined using Pierce BCA protein assay, and the same amounts of proteins were separated using SDS-PAGE gels. Proteins were transferred to a nitrocellulose membrane or a PVDF membrane and blotted with the corresponding antibodies. Blocking was performed in 5% dry milk/TBST, and antibody incubation was in 1% dry milk/TBST.

QUANTIFICATION AND STATISTICAL ANALYSIS

Hierarchical clustering and heat maps

The normalized abundances of metabolites were log-transformed, centered about the median, and clustered by Euclidean distance measure and Ward clustering algorithm using MetaboAnalyst 5.0, a web-based analysis platform (Pang et al., 2021) for hierarchical clustering analysis.

Statistical analysis

The statistical significance in corresponding figures was assessed using the Student's t-test. p values and *n* in column plots from Student's t-test were specified in the related figure legend.